An Ecological Perspective on Dolomite Formation in Great Salt Lake, Utah

Eric C. Dunham[1], Elizabeth M. Fones[1], Yihang Fang[2], Melody R. Lindsay[1],
Christopher Steuer[3], Nicholas Fox[3], Madelyne Willis[4], Alatna Walsh[3], Daniel R. Colman[1],
Bonnie K. Baxter[5], David Lageson[3], David Mogk[3], Andrew Rupke[6], Huifang Xu[2] and
Eric S. Boyd[1]*

[1] Department of Microbiology and Immunology, Montana State University, Bozeman, MT, United States, [2] Department
of Geoscience, University of Wisconsin-Madison, Madison, WI, United States, [3] Department of Earth Sciences, Montana
State University, Bozeman, MT, United States, [4] Department of Land Resources and Environmental Sciences, Montana State
University, Bozeman, MT, United States, [5] Great Salt Lake Institute, Department of Biology, Westminster College, Salt Lake
City, UT, United States, [6] Utah Geological Survey, Salt Lake City, UT, United States

Protodolomite was detected in sediments from Great Salt Lake (GSL), Utah, United States, that have no history of elevated temperature or pressure, conditions that are thought to promote dolomitization of sedimentary carbonates. Protodolomite was abundant in a non-oolitic sediment core from the South Arm (SA) of GSL at < 17% salinity but was rare in an oolitic sediment core collected from the North Arm (NA) of GSL at > 26% salinity. Protodolomite was also abundant in a non-oolitic NA sediment hand sample yet was absent in a nearby oolitic sediment hand sample in locations that likely receive allochthonous nutrients. Protodolomite was not detected in benthic photosynthetic mats from the SA. However, the mats comprised aragonite with halite and minimal calcite; benthic photosynthetic mats do not form in the NA. To begin to identify potential controls on the formation of protodolomite in the SA and NA of GSL, the composition and abundance of 16S rRNA gene transcripts, carbon cycling activities, and porewater geochemistry of the sediment cores were characterized. Transcripts affiliated with a dominant halophilic, heterotrophic sulfate-reducing bacterium were detected in the uppermost sections of the SA core and their abundance was positively correlated with rates of acetate oxidation/assimilation and concentrations of sulfide. Differences in the quality of organic matter between the SA and NA cores, as indicated by carbon to nitrogen ratios, indicate fresh deposition of photosynthetic biomass at the SA sediment core site but not in the NA sediment core site. Sediment grains from the SA core exhibit micrometer-sized euhedral protodolomite crystals that were not detected in the NA core. Collectively, these observations suggest that deposition of photosynthetic biomass drives the development of a sharp, anoxic lens of heterotrophic sulfate reduction. Sulfide, in turn, may promote dehydration of Mg^{2+}-water complexes and primary protodolomite nucleation and growth. The scarcity of dolomite in the NA sediment core may result from constraints imposed by a combination of extreme hypersalinity and depositional environment on phototrophs and sulfate reducers, their activities, and the thermodynamics of protodolomite formation.

Keywords: aragonite, dolomite, dolomitization, biomineralization, hypersaline, salinity, sulfate reduction, photosynthesis

INTRODUCTION

Dolomite [CaMg(CO$_3$)$_2$] is common in ancient sedimentary rocks of marine origin and is generally thought to have formed through diagenetic processes involving high temperature and pressure or through post-depositional replacement of calcite or aragonite (CaCO$_3$) (Rosenberg and Holland, 1964; Rosenberg et al., 1967; Hardie, 1987). The crystal structure of dolomite differs from that of calcite in that the ordering of calcium (Ca^{2+}) and magnesium (Mg^{2+}) ions into alternating layers results in reduced crystal symmetry (Gregg et al., 2015). Prior studies have distinguished high- and very-high-magnesium calcite [HMC, ∼4–25% MgCO$_3$ content; VHMC, 25–36% MgCO$_3$ content; both without cation ordering (Gregg et al., 2015)] from protodolomite (> 36% MgCO$_3$, weak cation ordering) and dolomite (> 36% MgCO$_3$ and strong cation ordering) (Fang and Xu, 2019). It has been demonstrated that VHMC formation always precedes the formation of ordered dolomite in high-temperature laboratory synthesis experiments (Gregg et al., 2015). While common in older rocks, dolomite and protodolomite are rare in modern marine sediments despite waters being supersaturated with respect to these minerals, which should favor their formation (Fairbridge, 1957). Albeit rare, dolomite and/or protodolomite have been detected in some modern day sedimentary environments that have no history of high temperature or pressure, including marginal hypersaline environments (e.g., Alderman, 1958; Vasconcelos et al., 1995; Van Lith et al., 2002; Pace et al., 2016) and evaporitic environments (e.g., Wells, 1962; Bontognali et al., 2010), among others.
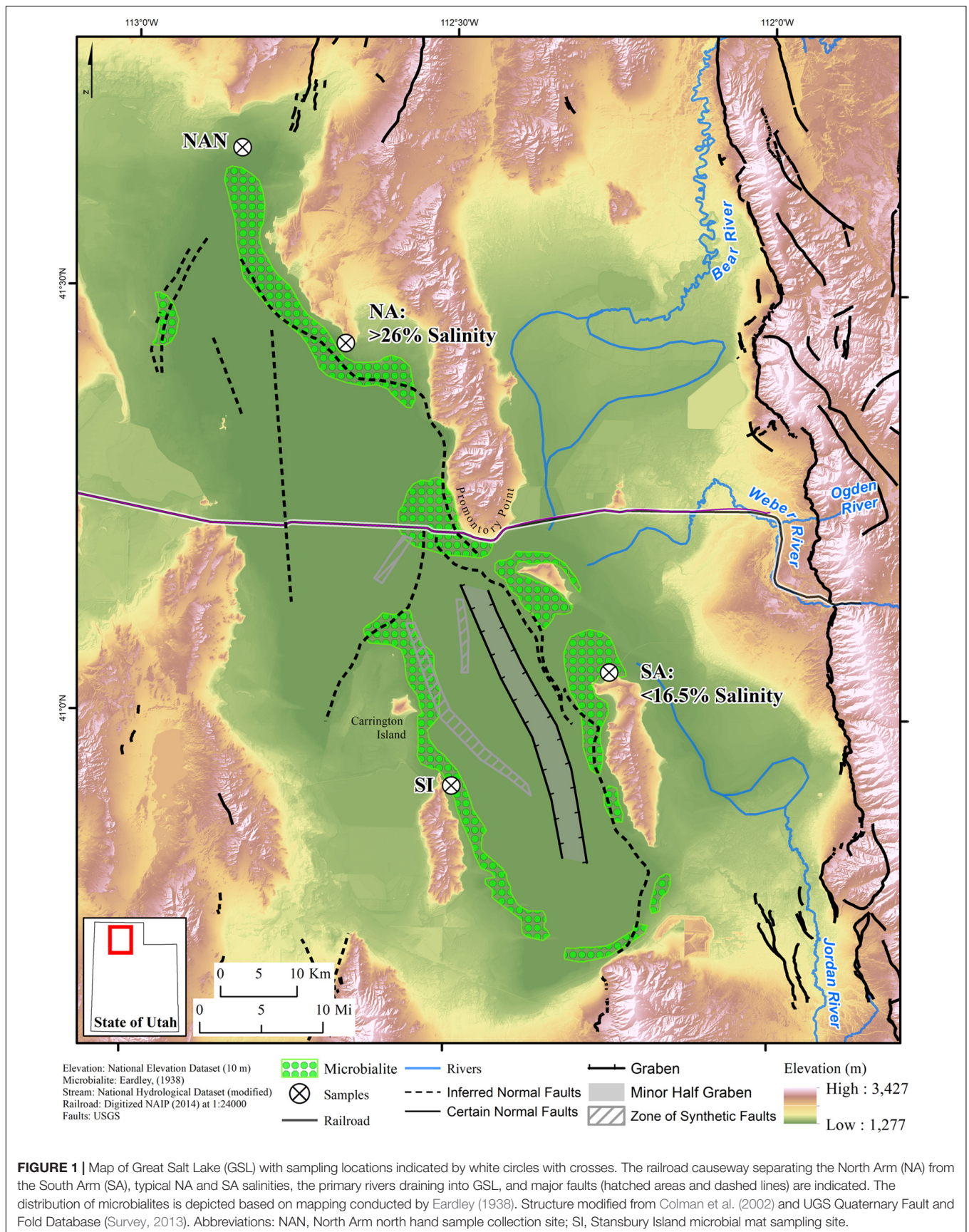
Various thermodynamic, kinetic, chemical, biological, and hydrological factors have been proposed to explain the formation of dolomite in modern day environments (Machel and Mountjoy, 1986). For example, it has been suggested that dolomite could form abiotically in saline environments with water chemistries above thermodynamic saturation with respect to dolomite (e.g., many saline to hypersaline environments), that are alkaline due to microbial activity, and that feature elevated temperatures (Machel and Mountjoy, 1986). Others suggest that biology is a key factor in dolomite formation (Vasconcelos et al., 1995) via either metabolic activities (Vasconcelos and Mckenzie, 1997; Van Lith et al., 2002; Moore et al., 2004; Kenward et al., 2009; Lu et al., 2018) or components of cells [e.g., extracellular polymeric substances (EPS) (Bontognali et al., 2010; Zhang et al., 2012b; Shen et al., 2015; Lu et al., 2018)] that create localized geochemical conditions or nucleation points, respectively, that are potentially favorable for dolomite formation. In particular, the activity of sulfate (SO$_4{}^{2-}$) reducing bacteria (SRB) can reduce the availability of SO$_4{}^{2-}$, which decreases ion pairing with Mg^{2+}, potentially making it more available for replacement of Ca^{2+} in calcite or aragonite (Baker and Kastner, 1981; Vasconcelos and Mckenzie, 1997; Warthmann et al., 2000; Bontognali et al., 2010). Alternatively, it has been suggested that removal of SO$_4{}^{2-}$ has little effect on the potential for dolomite formation, but rather it is the accumulation of sulfide from SRBs that promotes formation of this mineral (Zhang et al., 2012a, 2013; Lu et al., 2018). In this role, sulfide is thought to adsorb to calcite facies,

thereby reducing the energy required for dehydration of Mg^{2+}-water complexes on the same surfaces. Still others have suggested that salinity [e.g., sodium chloride (NaCl)] can exert strong influence on dolomite formation. For example, salinity may negatively influence the potential for dolomite formation since increased NaCl can promote complexation of Mg^{2+} and Ca^{2+} with SO$_4{}^{2-}$ and Cl$^-$ (Machel and Mountjoy, 1986), thereby rendering Mg^{2+} less available for dolomite formation. However, high salinities, in combination with high Ca^{2+} to Mg^{2+} ratios and SO$_4{}^{2-}$ reduction (SR) activity, have been associated with the formation of dolomite in several hypersaline systems (e.g., Van Lith et al., 2002).

SO$_4{}^{2-}$ reducing bacteria are common to many of the contemporary hypersaline environments where dolomite has been detected, including Great Salt Lake (GSL), Utah, United States (Brandt et al., 2001; Boyd et al., 2017). GSL is a hypersaline, terminal lake in the western United States (Hassibe and Keck, 1991) that exhibits a range of salinities due to localized freshwater input (∼95% of the total) into its southern end (Gwynn, 1996; Belovsky et al., 2011). Between 1900 and 1959, the salinity in GSL ranged, on average, from 20 to 27% (Stephens, 1990). In 1959, a rock and gravel railroad causeway was constructed, dividing the lake into two "arms" termed the North Arm (NA) and the South Arm (SA) (Cannon and Cannon, 2002) (**Figure 1**). Restricted water flow between these two arms due to the construction of the causeway has resulted in salinities that reach saturation (> 30%) in the NA and are < 20% in the SA, with localized areas of reduced salinity attributable to freshwater input (Baxter et al., 2005).

SO$_4{}^{2-}$ reducing bacteria are abundant components of benthic sediment communities in GSL (Boyd et al., 2017) and can reach densities of 10^7–10^8 cells cm^{-3} sediment (Brandt et al., 2001). The ecological success of SRB in GSL is likely due, in part, to elevated concentrations of SO$_4{}^{2-}$ in the lake that can exceed 30 g L^{-1} (Brandt et al., 2001; Gwynn, 2007; Boyd et al., 2017). Additionally, productive phototrophic plankton communities in the overlying water column (Post, 1977; Wurtsbaugh et al., 2011; Lindsay et al., 2017) can deliver fresh biomass to the benthos to support heterotrophic respiration. Finally, thick (∼1 cm) phototrophic, benthic microbial mats are commonplace along the shallow margins of the lake (Bouton et al., 2016; Pace et al., 2016; Lindsay et al., 2017, 2019) and may serve as an additional source of organic carbon capable of supporting heterotrophic SRB (Lindsay et al., 2019).

Previous studies have shown that the rate of SR is three orders of magnitude lower in sediments from GSL at elevated salinity (27% salinity) than in those at lower salinity (12%) (Brandt et al., 2001). Likewise, estimates of the abundance of cells performing SR and the abundance of 16S rRNA transcripts affiliated with SRB in sediments collected from hypersaline GSL locations were several orders of magnitude lower than those in less saline conditions (Brandt et al., 2001; Boyd et al., 2017). Activities of SRB sampled from hypersaline sediments in GSL increased when the salinity was artificially diluted, indicating that these populations are not well adapted to high salt conditions (Brandt et al., 2001). Importantly, benthic phototrophic microbial mats are estimated to contribute up to 30% of the productivity in

FIGURE 1 | Map of Great Salt Lake (GSL) with sampling locations indicated by white circles with crosses. The railroad causeway separating the North Arm (NA) from the South Arm (SA), typical NA and SA salinities, the primary rivers draining into GSL, and major faults (hatched areas and dashed lines) are indicated. The distribution of microbialites is depicted based on mapping conducted by Eardley (1938). Structure modified from Colman et al. (2002) and UGS Quaternary Fault and Fold Database (Survey, 2013). Abbreviations: NAN, North Arm north hand sample collection site; SI, Stansbury Island microbial mat sampling site.

the SA of GSL (Wurtsbaugh et al., 2011). Benthic phototrophic mats are not known to exist in the NA of GSL (Lindsay et al., 2017), likely due to constraints imposed by salinity on the primary architect of these mats, Cyanobacteria within the genus *Euhalothece* (Garcia-Pichel et al., 1998; Lindsay et al., 2017, 2019). The absence of benthic phototrophic mats, and therefore low levels of inorganic carbon fixation, in the NA may place constraints on the delivery of organic carbon capable of supporting heterotrophic SR in benthic sediments.

Previous studies have documented precipitation of aragonite in microbial mats (e.g., Reid et al., 2000; Schneider et al., 2013), including those that inhabit the SA of GSL (Pace et al., 2016). In GSL, aragonite precipitation was suggested to be localized to portions of the mat where SRB are actively degrading components of cyanobacterial biomass (Pace et al., 2016). However, other studies based on 16S rRNA gene (Lindsay et al., 2017, 2019) and transcript sequencing (M.R. Lindsay, *unpublished data*), the latter of which was conducted over a diel cycle, indicate that SRBs comprise only a minor portion (< 2–3%) of the communities associated with mats sampled from Bridger Bay in GSL, very close to where the previous study was conducted. Pace et al. (2016) also suggest that extracellular organic matter within the photosynthetic community may serve as a point of nucleation for aragonite mineral precipitation and growth (Pace et al., 2016). Moreover, it was suggested that partial replacement of aragonite with dolomite may take place within the mat (Pace et al., 2016), leading to dolomite preservation in benthic organo-carbonate structures dated to ~2000 to 10,000 BP (Bouton et al., 2016) that cover ~300 and 700 km^2 of the NA and SA lake bed (Eardley, 1938; Baskin, 2014).

In the present study, we sought to further characterize the role of microbial processes in the formation of dolomite in GSL. Specifically, we hypothesized that an abundant supply of SO_4^{2-} in sediment porewaters and infusion of nutrient-rich photosynthate and photosynthetic biomass from microbial mats promotes heterotrophic SR activity, which in turn promotes precipitation of VHMC and, potentially, (proto)dolomite. Moreover, it was hypothesized that (proto)dolomite would be more prevalent in the SA when compared to the NA due to constraints imposed by salinity on the productivity of the NA ecosystem (Lindsay et al., 2017, 2019), the activity and abundances of SRB (Brandt et al., 2001; Boyd et al., 2017), the availability of Mg^{2+} ions (Machel and Mountjoy, 1986), or a combination of these factors. To address these guiding hypotheses, a variety of sediment and microbial mat hand samples were collected from the SA and NA of GSL and these were subjected to mineralogical analyses. In addition, half meter sediment cores were collected from the SA and NA of GSL and these were subjected to mineralogical and porewater geochemical analyses. In parallel, rates of microbial inorganic carbon assimilation (primary production), microbial acetate mineralization and assimilation (secondary production), and quantities and compositions of archaeal and bacterial 16S rRNA gene transcripts were determined. Results are discussed in the context of the potential interplay of biological and abiological factors in the formation of carbonate minerals [i.e., aragonite, (proto)dolomite].

MATERIALS AND METHODS

Sampling Locations

Four sediment cores were collected from GSL for detailed characterization: two from the NA and two from the SA (**Figure 1**). The NA cores were collected offshore and a few hundred meters northwest of Spiral Jetty (41.43783°, −112.67103°). The NA sampling site is a west facing shoreline. The SA cores were collected offshore of Antelope Island Marina (41.06117°, −112.24531°) in a north facing bay that is protected from the rest of the lake by a small point extending into GSL called Ladyfinger. These locations were selected for several reasons: (*i*) both sample locations are along the GSL Fault Zone and represent marginal lake facies, (*ii*) both sample locations have microbialites (Eardley, 1938), although the NA microbialites have previously been inferred to no longer be actively forming (Lindsay et al., 2017), and (*iii*) both sampling sites are near wave base. However, the SA site is partially sheltered from wave activity by Ladyfinger Point (**Figure 1**).

Two sediment hand samples (top 5–8 cm) were collected from a playa in the northern most extension of the NA in GSL, termed Spring Bay (41.664801°, −112.836629°), on 9 April 2019 (**Figure 1**). These sediments were chosen since they, unlike the other NA sampling location, are likely to be influenced by seasonal input of organic matter. However, despite being only approximately 3 m apart, they exhibited different textures, as described below. These samples, termed NA North 1 and 2 (NAN-1 and NAN-2, respectively), were kept cool after transport to the lab where they were stored at −20°C.

Benthic microbial mats were collected from water column depths of no more than 0.5 m in several locations in the SA; benthic mats do not form in the NA. These hand samples include mats collected from Antelope Island 24 m to 8 km from the sediment core sampling site (depicted as SA on map; 41.06132°, −112.24510°) and Stansbury Island (depicted as SI on map; 40.91731°, −112.49111°) on 15 and 16 August 2016, respectively (**Figure 1**). Mat samples labeled Windward West, Bridger Bay, Buffalo Point, and Ridges were collected from the Antelope Island sampling location. All mat samples were collected aseptically, frozen on site using dry ice, and kept at −80°C prior to analyses.

Sample Collection and Field-Based Analyses

The duplicate NA sediment cores were collected on 9 May 2016 and the SA cores on 12 May 2016. Cores were collected ~3 m apart at each location, and each core was taken from an area of sediment submerged ~10 cm beneath the surface of the water and ~5 m from the shoreline. Cores were taken from areas interstitial to existing microbialite structures. PVC pipes (6.3 cm diameter) were driven into the sediment to a depth of 50 cm from the sediment–water interface. Cores were removed while minimizing sediment loss. One PVC pipe used at each sample site had pre-drilled holes stoppered with butyl rubber stoppers at 5 cm intervals. These cores were stored upright on ice within a cooler during transport to the laboratory where they were stored at 4°C and used to assess microbial activities within 1 week of

collection (described below). The second core from each site was frozen upright with dry ice on site and remained frozen during transport to the lab, where it was transferred to a −80°C freezer. These cores were sectioned into 5 cm segments (i.e., pucks) in a −20°C facility using a sterilized band saw. Core pucks were then halved, with one half reserved for stratigraphic, mineralogical, and image analyses and the other half reserved for molecular microbiological and pore water chemical analyses. Half-pucks were stored in sterile Whirl-Pak sampling bags at −80°C.

Field measurements on water overlaying the core sampling sites were conducted prior to core collection. Temperature and pH were measured using a YSI pH100CC-01 temperature compensated pH meter (YSI Inc.). Conductivity and total dissolved solids (TDS) were measured using a temperature-compensated YSI EC300 conductivity meter. Field measurements were not made for waters overlaying NAN-1 and NAN-2 sediments or SA microbial mats.

Core Descriptions

Half-cores reserved for mineralogy were subsampled for lithologic description. Individual samples were cut in centimeter increments with an X-Acto knife. Cuttings were then examined using a Nikon SMZ645 Model C-DS optical microscope.

Mineralogical Analysis

The NA and SA sediment columns were subsampled with 1.1 mm diameter Durafilm Kapton Tubing at 1–3 cm intervals. Multiple samples were taken at each depth without drying the columns to minimize sampling bias and avoid further halite precipitation. Individual sample-containing Kapton tubes were sealed at both ends with playdough to prevent dehydration during XRD analysis. Samples were then analyzed with the Rigaku Rapid II X-ray diffraction system (Rigaku Corporation, Tokyo, Japan) with Mo Kα radiation. This XRD instrument uses a 2-D image-plate detector for signal collection and integration using Rigaku's 2DP software. X-ray diffraction (XRD) experiments were run at 50 kV with a 100-μm diameter collimator. Mineral phases were identified using Jade 9.0 software. Mineral assemblages were calculated based on Rietveld refinement using TOPAS software with crystal structures from the American Mineralogist Crystal Database (AMCSD). Pearson VII peak were used for all refinements. Scanning electron microscopy (SEM) and energy-dispersive X-ray spectroscopy (EDS) were performed using a Hitachi S3400 (Hitachi, Ltd., Tokyo, Japan) with the Oxford EDS system (Oxford Instruments, Abingdon, United Kingdom). Samples for SEM were prepared by putting powder on carbon tape and then coating with 1 nm iridium.

For the purposes of this study, the $CaMg(CO_3)_2$ terminology laid out in Fang and Xu (2019) is used. To this end, the ordering state parameter s* was calculated for each analyzed sample:

$$s^* = 2x_{Mg} - x_{Mg-max}$$

Where x_{Mg} is the occupancy of Mg at Mg sites in the mineral lattice and x_{Mg-max} is the maximum occupancy allowed by the mol% $MgCO_3$ of the sample. Here, VHMC will refer to Ca-Mg carbonate with 25–36% $MgCO_3$ and no cation ordering (s* = 0), and "protodolomite" will refer to Ca-Mg carbonate with

> 36% $MgCO_3$ and weak-to-moderate cation ordering (0 < s* < x_{Mg-max}). "Dolomite" will be reserved for reference to Ca-Mg carbonate with >36% $MgCO_3$ and strong cation ordering (s* = x_{Mg-max} for Ca-rich dolomite, where $x_{Mg-max} \leq 1$; s* = x_{Ca-max} for Mg-rich dolomite, where $x_{Ca-max} \leq 1$).

Total Organic Carbon (TOC) and Total Nitrogen (TN)

Subsamples of sediment hand samples and select core subsections were thawed at 4°C overnight and then subsamples (∼0.2 g of wet weight sediment) were incubated at 90°C for 12 h to remove excess water. Dried samples were homogenized with a mortar and pestle and fumed with 12 N HCl for 24 h in a hermetically sealed glass container. Samples were dried once more at 90°C for 12 h prior to transfer to individual tin cups, weighing, and analysis on a Thermo Finnigan FlashEA 1112 nitrogen and carbon analyzer (Macdonald et al., 2018). TOC and TON were normalized to grams dry weight sediment.

Sediment Porewater Characterization

Subsamples of ∼5 g were removed from each frozen core section using a scroll saw in a −20°C facility. The wet mass of one such sample was determined, and then the tube was uncapped and placed in a 90°C drying oven. After 48 h in the oven, the sample was weighed again to obtain its dry mass. Water content was calculated as percent of mass lost during drying.

pH and NaCl concentrations were measured in a second subsample of each core. Core sediments formed a thick mud when they were thawed making it difficult to separate a supernatant. Therefore, subsamples were added to 15 mL conical tubes containing 3 mL diH$_2$O. Thawed sediment slurries were mixed by vortexing, followed by centrifugation at 4000 × g for 15 min. The refractive index of one aliquot of each clarified supernatant was measured with a Reichert AR200 handheld digital refractometer (Reichert Technologies). Since GSL is primarily a NaCl lake (Oren, 2013), the refractive indices were converted to NaCl concentrations using a NaCl standard curve. Another aliquot from the supernatant described above was used to measure pH using an Accumet AB150 pH probe. Sulfate concentrations were determined using the barium sulfate turbidity method (Burlage et al., 1998). Sulfate standards were prepared using sodium sulfate decahydrate (Na$_2$SO$_4$ · 10H$_2$O) in solutions of NaCl at concentrations specific to each sediment core.

Sulfide concentrations were determined in a third subsample of each frozen core section added to a 50 mL conical tube. To minimize sulfide oxidation, tubes were flushed with 60 mL N$_2$ gas, capped, and stored in a −80°C freezer prior to analysis. To measure sulfide in sediment porewaters while minimizing turbidity that interferes with the measurements, tubes were brought into an anaerobic chamber where 5 mL anoxic water was added to each to thaw and suspend sediments. As soon as samples had completely thawed, they were centrifuged at 4600 × g for 5 min. Once the spin was complete, the concentration of total dissolved sulfide in the supernatant was immediately determined by the methylene blue reduction method (Fogo and Popowsky, 1949). Standard curves were generated with sodium sulfide

(Na$_2$S) solutions made at NaCl concentrations specific to each sediment core. Sulfide concentration was calculated based on the water content of sediments and dilution by the added diH$_2$O. The amount of sulfide reported is likely a minimum estimate considering the potential for degassing and/or oxidation during the preparation of the sample and does not account for mineral sulfides that might have been present in the particulate fraction of the sediment cores.

Dissolved gases other than sulfide were measured using a fourth subsample added to a 60 mL syringe sealed with a stopcock, using previously described methods (Fendinger and Adams, 1986). Briefly, the headspace of the syringe was flushed with high purity nitrogen (N$_2$) gas five times before 10 mL anoxic zinc acetate solution was added (final concentration of 0.1 M) to precipitate any sulfide that might be present and to provide sufficient supernatant for equilibration of analytes between liquid and gas phases. A 10 mL volume of high purity N$_2$ gas was then added to the syringe. The subsample was thawed and was then shaken vigorously for 1 min by hand. The 10 mL gas volume was then removed and transferred to a pre-evacuated Cali Bond gas-sampling bag (Calibrated Instruments, Inc.) that had been flushed three times with high purity N$_2$ gas.

Five mL of gas from each Cali Bond gas sampling bag was injected into an SRI 8610C gas chromatograph (SRI instruments) as previously described (Lindsay et al., 2018). Hydrogen (H$_2$), carbon dioxide (CO$_2$), and methane (CH$_4$) were separated on a 4.5 m × 0.125" OD Hayesep DB 100/120 packed column (Valco Instruments Company, Inc.). Helium was used as the carrier gas. Gas sample concentrations were calculated using a standard curve (1–10,000 ppm calibration range) generated daily using certified (± 5%) standards (American Gas Group). Gas phase concentrations were converted to dissolved aqueous phase concentrations according to Henry's law, as previously described (Spear et al., 2005). Concentrations were normalized to mean sediment pore water content for each core (35.4 and 13.4% water by mass for SA and NA, respectively).

Carbonate Saturation Indices

Saturation indices for aragonite and dolomite were calculated for both the NA and SA over a range of historical geochemical conditions in GSL using PHREEQc (Saini-Eidukat and Yahin, 1999; Parkhurst and Appelo, 2013). Historical GSL water column alkalinity measurements were collected from prior publications (Stephens and Gillespie, 1976; Post, 1977; Gwynn, 1980; Post, 1981; Jones et al., 2009; Pace et al., 2016) and the minimum, maximum, and average values were determined for use in modeling (**Supplementary Table S1**). Historical GSL water column chemical data were obtained from the USGS GSL Brine Chemistry Database (Rupke and Mcdonald, 2012) using the 30 May 2017 revision, and the minimum, maximum, and average values for select sites were determined for use in modeling (**Supplementary Table S2**).

The maximum, minimum, and average historical saturation indices in the NA and SA of GSL (**Supplementary Table S3**) were calculated with the maximum, minimum, and average alkalinity and bulk water chemistry values (**Supplementary Tables S1, S2**). Data from Utah Geological Survey sites LVG4 (−112.7616, 41.3240) in the NA and AS2 (−112.2558, 40.8349) in the SA were

selected because they possessed the longest and most complete datasets over the period of 1966–2017. Saturation indices for aragonite and dolomite in the bulk water column were calculated at 32°C (historic maximum), 15°C (historic median), and 0°C (near freezing). The pH of the water column was fixed at 7.7 for LVG5 (NA) and 8.2 for AS2 (SA), as recorded previously (Post, 1977).

The median alkalinity for the NA or the SA was used along with the chemistry of overlying waters at Utah Geological Survey sampling sites SJ-1 (−112.6684, 41.4380) in the NA and AIS (−112.2544, 41.0146) in the SA on 1 July 2016 (**Supplementary Table S4**) to calculate aragonite and dolomite saturation indices as a function of bulk water column pH (**Supplementary Table S5**). These sites were selected for calculations of aragonite and dolomite saturation as a function of pH because they were located closest to our sampling sites and data were collected near to the time that samples analyzed in this study were collected. A surface water temperature of 26°C was invoked, as in a previous study (Pace et al., 2016), for calculations of aragonite and dolomite saturation indices.

Determination of Microbial Primary and Secondary Production/Activity in Core Sediments

Rates of dissolved inorganic carbon (DIC) assimilation and acetate assimilation/mineralization were determined as proxies for microbial primary production and secondary production/activity, respectively. Sediments were subsampled from the unfrozen SA core at the sediment-water interface and at settled depths scaling to 11.3, 22.5, 33.8, and 45.0 cm. Likewise, sediments were subsampled from the unfrozen NA core at the sediment–water interface and at depths scaling to 11.7, 23.3, 29.3, and 35.0 cm. Roughly 100 mg aliquots of sediment from each depth interval were added to sterile 24 mL serum bottles. After sediment addition, the bottles were capped with butyl rubber stoppers and purged with N$_2$ for ∼5 min. Sediments were then overlaid with 10 mL filter-sterilized, N$_2$ purged GSL water collected from the water column overlying each sampling location. Serum bottles and their contents were then degassed with N$_2$ for an additional 30 min. For each depth interval at each site, 15 replicate assays were prepared for measurement of DIC assimilation and 15 were prepared to measure acetate mineralization (see below).

Dissolved inorganic carbon assimilation rate potential assays were initiated by injecting 1.0 µCi of [^{14}C] sodium bicarbonate (NaH^{14}CO$_3$) to each serum bottle to achieve a final concentration of 2 µM NaH^{14}CO$_3$. Acetate mineralization and assimilation rate potential assays were initiated by injecting 0.5 µCi of [^{14}C] sodium acetate (^{14}CH$_3$COONa) to each serum bottle to achieve a final concentration of 1 µM. Fifteen assays for each ^{14}C source were set up for each depth interval and were incubated at temperatures corresponding to the overlying water at the time of sampling. Triplicate assays were removed following 1, 2, 4, 8, and 12 h of incubation at the specified temperature. The assays were then terminated by freezing at −20°C prior to analysis. Assays were processed for assimilation of inorganic carbon to biomass, assimilation of acetate to biomass, and oxidation of acetate

to CO_2 using scintillation counting as previously described (Urschel et al., 2015). Radioactivity was then measured in counts per minute (CPM) on a Beckman LS 6500 liquid scintillation counter (Beckman Coulter, Inc., Indianapolis, IN, United States) and converted to disintegrations per minute (DPM) using a quench curve. The average and standard error of the mean of three replicate assimilation assays are presented for the pair of incubation time points that showed the largest difference in substrate transformation. Separate samples of the inoculum were dried and weighed to determine the dry mass of the sediment in the sediment slurry that was added to each assay.

RNA Extraction and cDNA Synthesis

Duplicate samples of sediment were subsampled from frozen core sections with a sterile spatula after first scraping off the top layer (~3 mm). Samples were allowed to thaw before they were subjected to RNA extraction, DNAse treatment, quantification, and conversion to cDNA, as described previously (Lindsay et al., 2018). cDNA was subjected to amplification of archaeal, bacterial, and eukaryal small subunit rRNA gene transcripts using the primer sets 344F/915R, 1100F/1492R, and A7F/570R, respectively, as previously described (Hamilton et al., 2013). Quantitative PCR (qPCR) of 16S/18S rRNA gene transcripts was performed as previously described (Lindsay et al., 2018) using plasmid standards previously constructed using amplicons from GSL (Lindsay et al., 2017). Negative control reactions were performed in the absence of added cDNA.

Eukaryal amplicons were not detected in cDNA via PCR or qPCR. Archaeal and bacterial 16S cDNA amplicons were barcoded and sequenced with the 2 × 300 MiSeq Reagent Kit v3 following the manufacturer's instructions, as described previously (Lindsay et al., 2018). Post sequence processing was performed with Mothur (ver. 1.36.1) (Schloss et al., 2009) as previously described (Hamilton et al., 2013) after merging the paired reads. Merging was only conducted for bacterial reads; archaeal reads were not merged due to poor overlap. Further details of how sequences were processed can be found in our previous publication (Lindsay et al., 2018). Following processing, a normalized size of 533 and 1809 16S cDNA sequences was obtained for each of the archaeal and bacterial libraries, respectively. Sequences specific for each operational taxonomic unit (OTU, classified at 97% sequence similarity) were classified using the Bayesian classifier of Mothur (Wang et al., 2007) and the RDP database (training set 14), with manual verification using BLASTn. The compositions of the forward and reverse reads for archaeal 16S rRNA gene transcript libraries were similar, and thus only the results of the forward reads are presented. Raw reads, quality scores, and mapping files for the archaeal and bacterial 16S rRNA gene transcript libraries have been deposited in the NCBI short reads archive under BioProject accession number PRJNA481529.

RESULTS

Sediment Sample Characteristics

Two sediment hand samples were collected from Spring Bay in the NA of GSL, NAN-1 and NAN-2. NAN-1 consisted primarily of rounded oolitic sand and playa mud while NAN-2 was primarily playa mud. In addition, sediment cores were collected for use in characterizing the chemical, mineralogical, and physical attributes of NA and SA sediments.

The NA sediment core measured approximately 40 cm in length (**Supplementary Figure S1**). Most of this core comprised rounded ooids, 0.5 mm or less in diameter, and enveloped in calcium carbonate and halite. Ooids had a dark, spotted texture beneath a coating of halite and calcium carbonate. These sediments were grain supported, loosely cemented, and lacked any matrix. The pH, temperature, specific conductivity, and TDS content of the water overlying the NA sediment column at the time of sampling were 7.50, 22.4°C, 207.2 mS, and 134.9 g L^{-1}, respectively.

The SA sediment core measured approximately 45 cm in length (**Supplementary Figure S1**). The core comprised planar mm–cm scale beds of alternating dolomitic to calcareous carbonate mud, clay, and silt particles with abundant salts. Occasional zones of stylolites occurred at bedding boundaries and black, dendritic precipitates existed throughout. Sediments were matrix supported, well-cemented, and contained orange-brown ooids typically less than 0.1 mm in diameter. The pH, temperature, specific conductivity, and TDS content of water overlying the SA sediment column at the time of sampling were 7.17, 30.5°C, 176.3 mS, and 103.9 g L^{-1}, respectively.
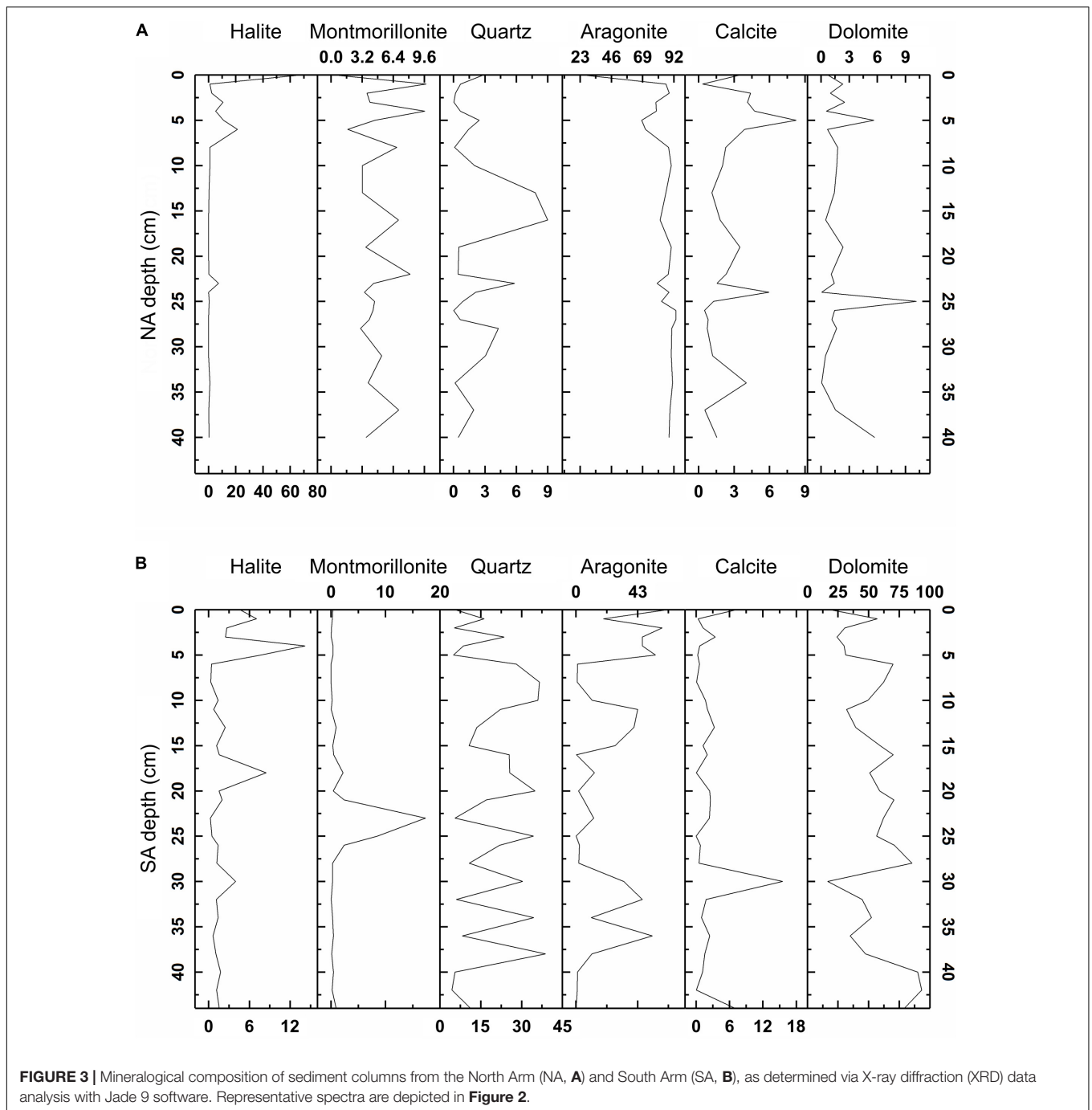
Sediment Column and Microbial Mat Mineralogy

X-ray diffraction revealed very different mineral assemblages among the sediment cores, sediment hand samples, and microbial mats (**Figures 2**, **3** and **Supplementary Table S6**). The NA sediment core was dominated by aragonite with varied amounts of VHMC, protodolomite, calcite, halite, and smectite, as was the NAN-1 hand sample (**Figures 2B**, **3A** and **Supplementary Table S6**). In contrast, sediment from NAN-2, collected only a few meters away from NAN-1, was dominated by protodolomite (**Supplementary Table S6**). The SA sediment core contained predominantly protodolomite with moderate amounts of quartz and aragonite and trace amounts of calcite, halite, and smectite (**Figures 2B**, **3B**). Microbial mat hand samples collected from the SA comprised mostly aragonite with halite and Mg-calcite (**Figure 2A** and **Supplementary Table S6**). None of the mat samples contained dolomite or even HMC. The protodolomite-dominated sediment samples (SA core and NAN-2) were each composed of very fine grain muds, while the aragonite-dominated samples (NA core and NAN-1) comprised micron-scale oolites.

Values of mineral lattice spacings (i.e., d_{104} values) of the protodolomite also varied with sediment depth, ranging from 2.883 to 2.931 Å in the NA and from 2.887 to 2.905 Å in the SA. Lower boundaries of mol% $MgCO_3$ were calculated based on an empirical d_{104} versus mol% $MgCO_3$ curve for complete ordered dolomite (Graf and Goldsmith, 1956; Reeder and Sheppard, 1984; Zhang et al., 2010; Fang and Xu, 2019). Based on this relationship,
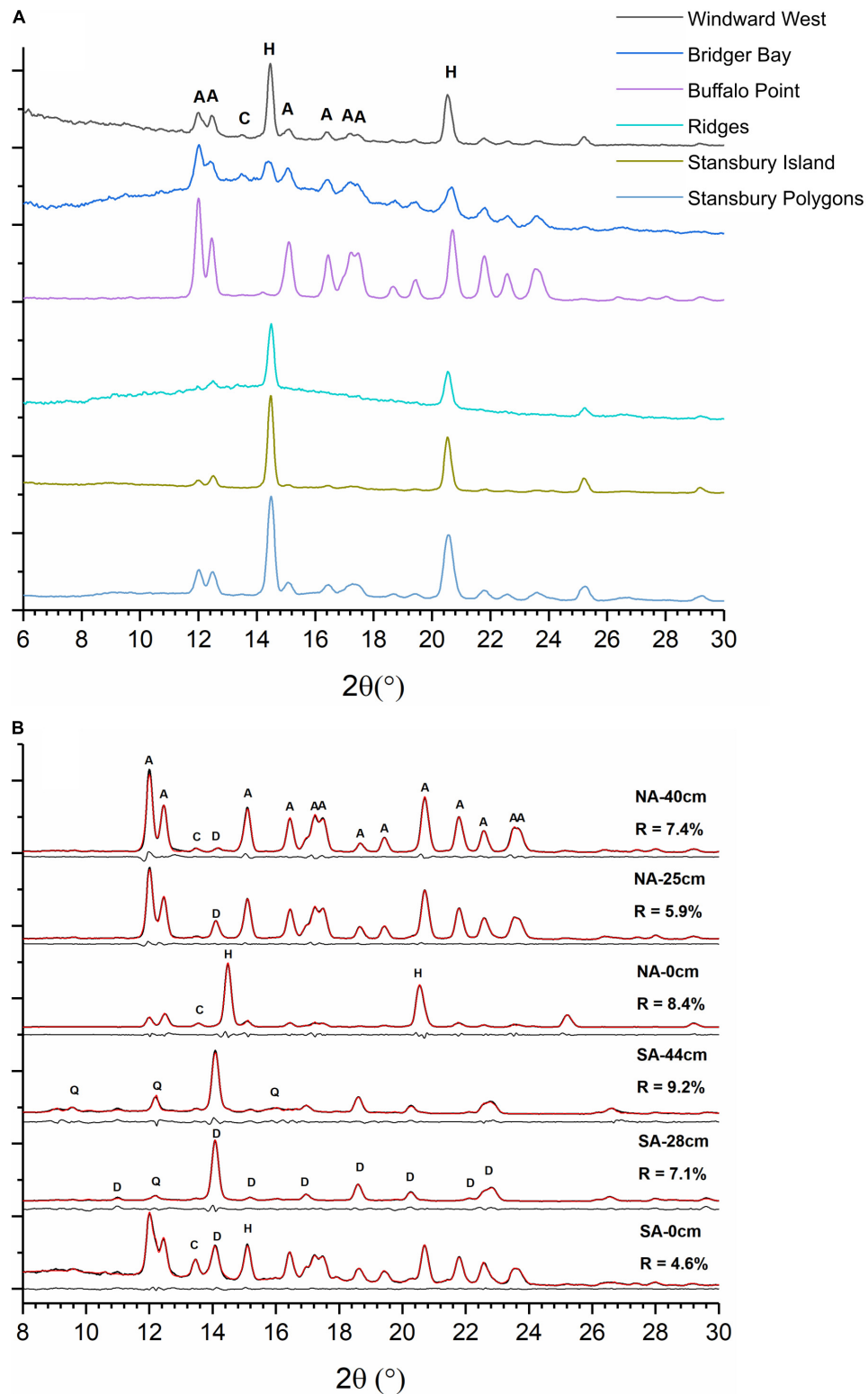
FIGURE 2 | (A) X-ray diffraction (XRD) patterns of microbial mats from the South Arm (SA) of Great Salt Lake (GSL). Mats are dominated by aragonite (A) and halite (H) with trace amount of calcite (C). **(B)** Representative XRD patterns of sediments from the North Arm (NA) and SA cores at indicated depths below the sediment–water interface. Thin red lines are refined results overlaid on black original data. Thin black lines below each pattern are residues from Rietveld refinement. NA sediments are dominated by aragonite, halite, and calcite, with trace amounts of high magnesian calcite/protodolomite (D). SA sediments are dominated by high magnesian calcite/protodolomite with small amounts of halite, calcite, and quartz (Q).

FIGURE 3 | Mineralogical composition of sediment columns from the North Arm (NA, **A**) and South Arm (SA, **B**), as determined via X-ray diffraction (XRD) data analysis with Jade 9 software. Representative spectra are depicted in **Figure 2**.

the NA core comprised at least 33 mol% $MgCO_3$ and the SA comprised at least 44% $MgCO_3$.

SEM

North Arm sediments were homogeneous under SEM throughout the 40 cm core and a substantial portion of grains had cubic halite crystals precipitated on their surfaces. These sediments contained well-rounded grains of ooids and pellets with crater-like textures (**Figures 4a,b**). Grain size ranged from 2–6 µm (methods and results described in the

Supplementary Material) and EDS revealed grain composition to be aragonite with VHMC or protodolomite regions cemented within (**Supplementary Figure S2**).

In contrast, SA core sediments exhibited euhedral crystals under SEM (**Figures 4c,d**), which were found to be consistent with aragonite and protodolomite by EDS analysis (**Supplementary Figure S3**). Rather than being cemented within oolites, protodolomite in the SA core formed micrites. These rhombohedral protodolomite grains were relatively free of accessory mineral growth on their crystal faces.
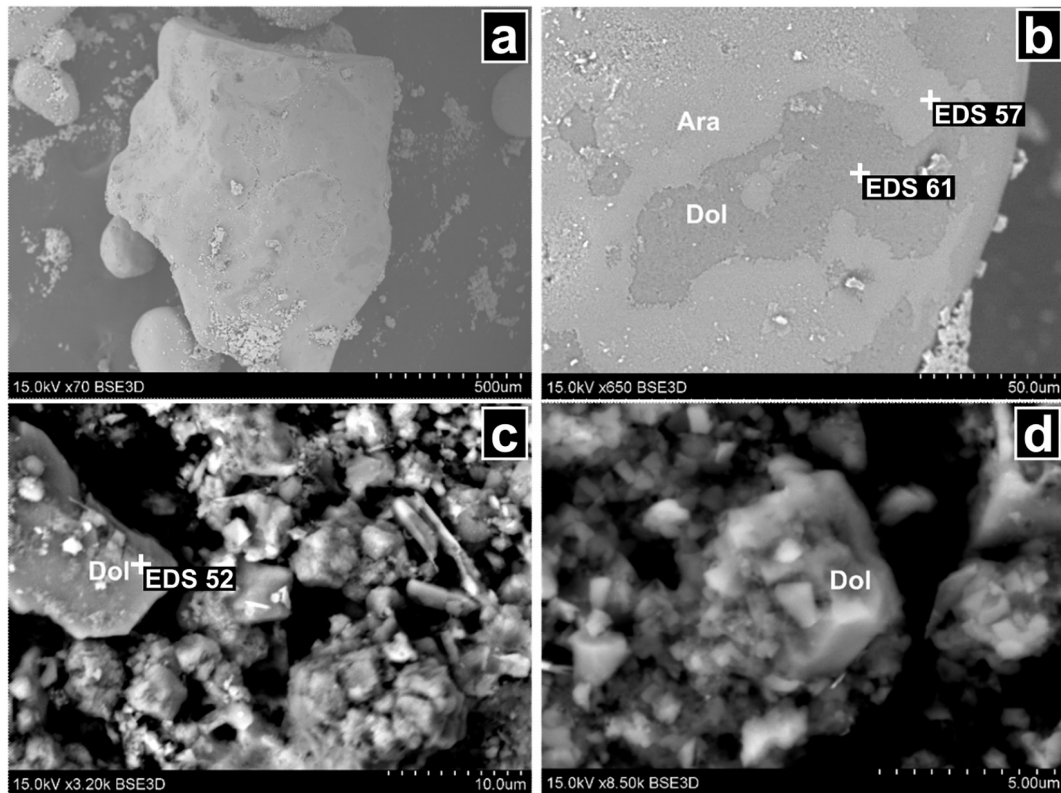
FIGURE 4 | Scanning electron microscopy (SEM) images of sediments from North Arm (NA) and South Arm (SA) cores. **(a)** Aragonite ooite from 1 cm depth in the NA core. **(b)** Increased zoom portion of **a** showing disordered dolomitic region in the aragonite ooite. **(c,d)** Euhedral protodolomite crystals from SA core, 0 and 24 cm in depth, respectively. Plus signs and labels indicate locations of energy dispersive X-ray spectroscopy (EDS) analyses, the results of which are presented in **Supplementary Figures S2, S3**. Abbreviations: Dol, dolomite; Ara, aragonite.

Dispersive X-ray spectroscopy results showed the majority of the protodolomite in each core to be Mg-rich. The NAN-1, NAN-2, SA-0 cm, and SA-24 cm samples had averages of 54.4, 47.9, 53.3, and 57.4 mol% $MgCO_3$, respectively. Together with the d_{104} values acquired through XRD analysis, these compositions indicate a consistent ordering state of s* = ~0.25 across all samples, as determined by previously published methods (Fang and Xu, 2019).

Sediment Porewater Geochemistry

The water content of the NA sediment column was always lower than that of the SA column, regardless of depth (**Supplementary Table S7**). While water content varied little with depth in the NA column (11–16% by mass), it was highly variable in the SA column (~20–50% by mass). The pH of sediment porewater was higher in the NA core than the SA core at all depth intervals sampled (**Supplementary Table S7**). Porewater pH ranged from 8.04 to 8.54 in the NA core and from 7.64 to 8.01 in the SA core. The pH gradually decreased in the NA between 0 and 30 cm in depth and then increased markedly at 35 and 40 cm. In contrast, SA porewater pH was largely consistent throughout the sediment core.
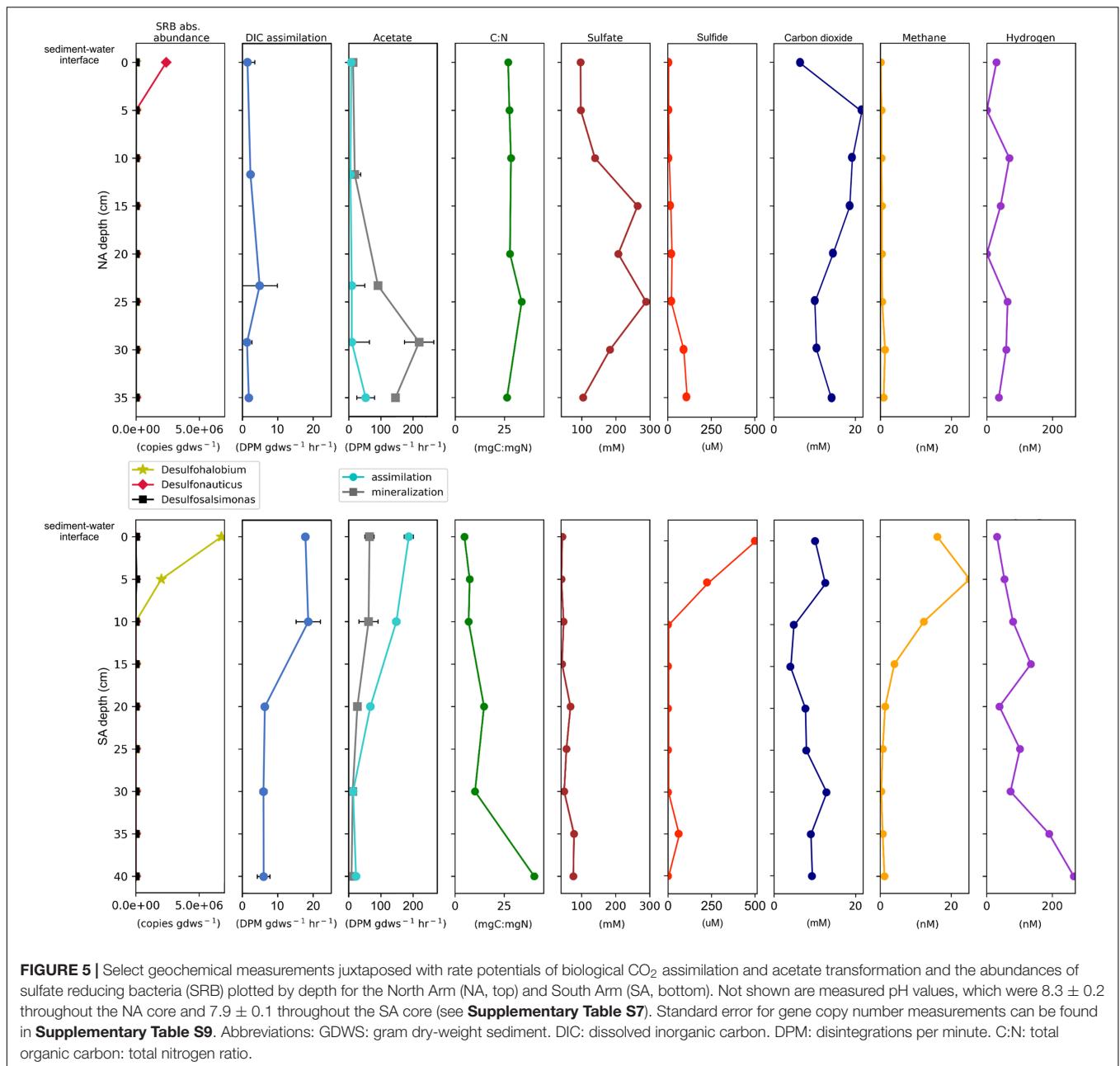
North Arm porewaters were saturated with respect to NaCl while salinity in the SA core ranged from 13.1 to 16.7% g mL^{-1}

(**Supplementary Table S7**). Listed values for the NA greater than the maximum solubility of NaCl resulted from the addition of deionized water to generate enough supernatant to measure with a digital refractometer. This addition allowed for dissolution of halite crystals (visible in the sediment core before manipulation).

Porewater dissolved gas profiles varied markedly as a function of depth both within and between sediment cores (**Supplementary Table S7** and **Figure 5**). In the NA, total dissolved sulfide increased with depth from 6 μM at the sediment–water interface to 110 μM at 35 cm. Porewater CH_4 concentrations in the NA core were uniformly low along the depth transect and never exceeded 2 nM.

Total dissolved sulfide in SA sediment porewater was 500 μM at the sediment–water interface and decreased precipitously to below 4 μM at 10 cm and lower, with a spike of 65 μM at 35 cm. CH_4 was detected at concentrations ranging from 15 to 20 nM between the sediment water interface and 10 cm depth, there after falling quickly to sub-nM concentrations by 25 cm and remaining at low levels.

Concentrations of dissolved H_2 in sediment porewaters from both the NA and the SA were highly variable, with higher concentrations typically observed at depth when compared to surface transects (**Supplementary Table S7** and **Figure 5**). In the NA, dissolved H_2 concentrations were similar along the depth

FIGURE 5 | Select geochemical measurements juxtaposed with rate potentials of biological CO_2 assimilation and acetate transformation and the abundances of sulfate reducing bacteria (SRB) plotted by depth for the North Arm (NA, top) and South Arm (SA, bottom). Not shown are measured pH values, which were 8.3 ± 0.2 throughout the NA core and 7.9 ± 0.1 throughout the SA core (see **Supplementary Table S7**). Standard error for gene copy number measurements can be found in **Supplementary Table S9**. Abbreviations: GDWS: gram dry-weight sediment. DIC: dissolved inorganic carbon. DPM: disintegrations per minute. C:N: total organic carbon: total nitrogen ratio.

profile and always below 75 nM. SA sediment porewater H_2 was present at $\sim$30 nM at the sediment–water interface and rose to $\sim$140 nM at 15 cm in depth. Between 15 and 20 cm porewater H_2 dropped to just 40 nM before rising gradually to over 250 nM at 40 cm.

The TOC to TN (C:N) ratio in sediments from the NA core did not fluctuate and remained $\sim$28 throughout (**Figure 5**). In contrast, C:N was low (4–5) in surface sediments of the SA core but then increased to $\sim$30 in deeper sediments. The increase in the C:N ratio with depth in the SA core was not due to large changes in TOC, but rather to decreases in TN (**Supplementary Table S7**). Overall, TOC was similar in the two cores, while TN was higher in the SA, especially at shallow depths. TOC and TN were 1.64 and 0.14%, respectively, in

the NAN-1 hand sample and were 0.15 and 0.02% in the NAN-2 sample. The C:N ratio was 7 in NAN-1 and 11 in NAN-2 sediments.

Abundance and Affiliations of Bacterial 16S rRNA Gene Transcripts

Bacterial 16S rRNA gene transcript abundances were similar in the NA and SA and relatively consistent throughout the sediment columns (**Supplementary Table S8**). In the NA column, bacterial transcripts were highest in the 0 cm section, declining gradually with depth to about 30-fold lower in the deepest (35 cm) section. SA transcripts were also highest in the 0 cm section but varied by less than an order of magnitude throughout.

A total of 1809 bacterial 16S rRNA gene transcript sequences were subsampled from libraries from each core section (**Supplementary Figure S4** and **Supplementary Table S8**). At the genus level, the bacterial communities in both cores at 10 cm depth and below were dominated by OTUs affiliated with *Sphingomonas* (**Supplementary Figure S4**). However, in the topmost sediments (0 and 5 cm core sections), *Sphingomonas* sequences were only minor components. The 0 and 5 cm core sections from the NA were dominated (83 and 61% of total reads, respectively) by OTUs that exhibited 93–96% sequence identity to sequences from uncultivated organisms affiliated with the phylum Acetothermia. A minor component (2.6%) of the OTUs from the NA 0 cm core section was affiliated (93–94% sequence identity) with the SRB *Desulfonauticus autotrophicus*. In the SA, OTUs accounting for 61 and 47% of the reads in the 0 and 5 cm core sections, respectively, exhibited 94–100% sequence identity to the SRB *Desulfohalobium utahense*.

We compiled OTUs that exhibited close affiliation with known SRBs and multiplied their relative abundances by the total abundance of bacterial transcripts at each depth with which that OTU was affiliated to determine the absolute abundance of templates affiliated with dominant OTUs (**Supplementary Table S8** and **Figure 5**). In the NA core, the predominant SRBs were affiliated with *Desulfonauticus* (10^6 copies gdws^{-1}) and, to a lesser extent, *Desulfohalobium* (10^3 copies gdws^{-1}). Templates affiliated with *Desulfonauticus* were only identified in the top section (0 cm) of the sediment column. In the SA, the predominant SRBs were affiliated with *Desulfohalobium* (10^6 copies gdws^{-1}) and to a lesser extent *Desulfosalsimonas* (10^4 copies gdws^{-1}), and these were most abundant in the 0–5 cm core sections. Data for the abundance and composition of archaeal transcripts, which will not be discussed in detail here, can be found in **Supplementary Figure S5** and **Supplementary Table S8**.

Rate Potentials of Microbial Primary and Secondary Production

Assimilation of DIC (primary production) was detected in communities associated with sediments from each NA and SA core section (**Supplementary Table S9** and **Figure 5**). Rates of DIC assimilation were low and did not change significantly with depth in the NA sediment core. In the SA, potential rates of DIC assimilation were up to four times higher than in the NA. These were highest at the sediment–water interface and at 10.0 cm depth, nearly double the rates measured in the bottom three depth intervals (22.5, 33.8, and 45.0 cm). As such, rates of DIC assimilation were inversely correlated with depth (Pearson $R = -0.86$).

Assimilation and mineralization of acetate (secondary production) were also detected in communities associated with sediments from each assayed core section (**Supplementary Table S9** and **Figure 5**). In the NA core, acetate mineralization was lowest at the sediment–water interface and increased with depth by several orders of magnitude, with the highest rate of acetate mineralization detected at a depth of 29.2 cm and the highest rate of acetate assimilation measured at a depth of 35.0 cm. Thus

NA sediments exhibited positive relationships between acetate mineralization/assimilation and depth (Pearson $R = 0.85$ and 0.64, respectively). Contrastingly, in the SA sediment core, rates of acetate mineralization and assimilation were highest in the top two depth intervals sampled (the sediment–water interface and at 10 cm depth). Rates then decreased with depth, with the lowest rate of mineralization measured at 40 cm and the lowest rate of assimilation at 30 cm. SA sediments thus exhibited inverse relationships between acetate mineralization/assimilation and depth (Pearson $R = -0.95$ and -0.94, respectively).

Aragonite and Dolomite Saturation Indices

The saturation indices of aragonite and dolomite were calculated based on lake conditions near sediment core collection sites. **Figure 6A** shows indices calculated using geochemical data collected July 1, 2016. Saturation indices were calculated as functions of pH across a range meant to capture conditions that might develop on a microscale in sediment porewaters.
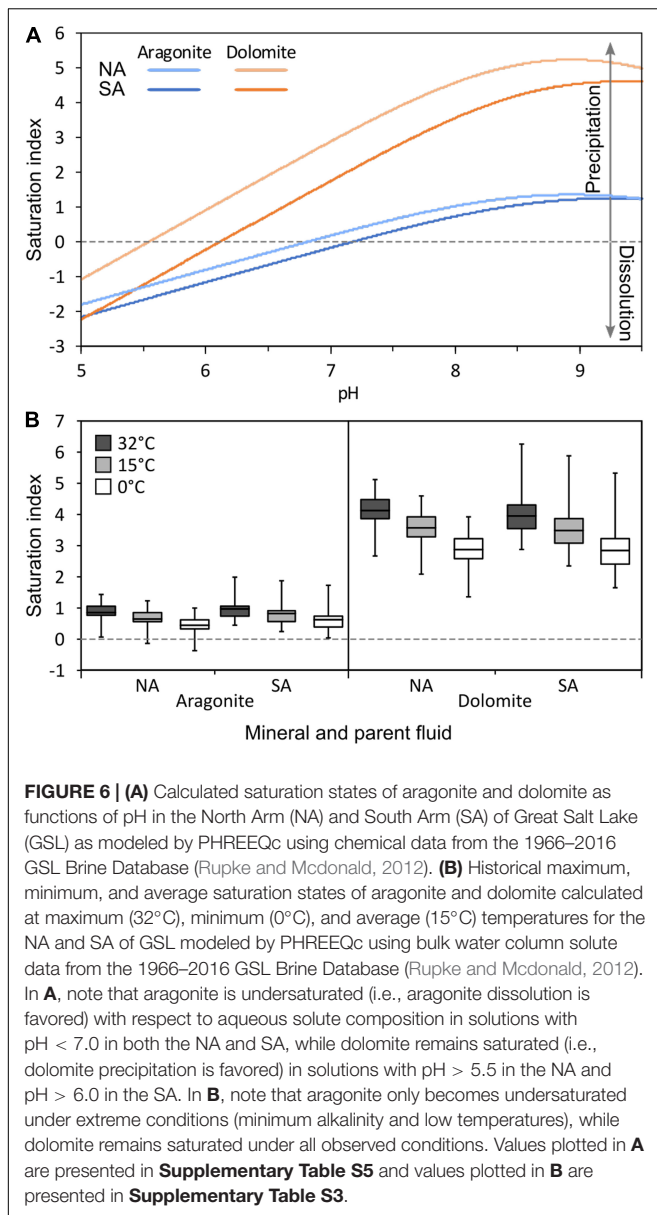
These calculations indicate that GSL was saturated with respect to both aragonite and dolomite (favoring mineral formation) through the whole pH range (7.64–8.54) observed in bulk NA and SA porewaters. However, saturation indices for both minerals decline with decreasing pH. The saturation index of aragonite falls below zero (undersaturation, favoring mineral dissolution) at pH < 6.7 in the NA and < 7.1 in the SA. The dolomite saturation index falls below zero at pH < 5.5 in the NA and < 6.0 in the SA. Thus, in the pH range 5.5–6.7 (NA) or 6.0–7.1 (SA), dolomite is thermodynamically stable while aragonite is predicted to dissolve.

To encompass historical variation in the geochemical conditions of GSL and to assess its effect on aragonite and dolomite saturation indices, data were compiled from locations in the NA and SA over the time frame 1966–2017 (**Figure 6B**). Historical ranges of water solute concentrations were used to calculate a minimum, average, and maximum saturation index for each mineral at the minimum, average, and maximum recorded temperatures. These calculations indicate that geochemical conditions have favored dolomite formation throughout this time frame in both the NA and SA. Conditions have also likely favored aragonite formation throughout this period, with its saturation index falling below zero only at the lowest recorded alkalinities and during the coldest intervals.

DISCUSSION

Proposed Model for Protodolomite Formation in GSL

A mechanism has been previously proposed to explain (proto)dolomite formation in phototrophic microbial mats in Bridger Bay, GSL (Pace et al., 2016). In this model, the activity of SRB drives aragonite precipitation within the mat structure. This biomass-associated aragonite is then deposited to sediments where dolomitization of aragonite takes place due to localized increases in acidity induced by fermentative

FIGURE 6 | (A) Calculated saturation states of aragonite and dolomite as functions of pH in the North Arm (NA) and South Arm (SA) of Great Salt Lake (GSL) as modeled by PHREEQc using chemical data from the 1966–2016 GSL Brine Database (Rupke and Mcdonald, 2012). **(B)** Historical maximum, minimum, and average saturation states of aragonite and dolomite calculated at maximum (32°C), minimum (0°C), and average (15°C) temperatures for the NA and SA of GSL modeled by PHREEQc using bulk water column solute data from the 1966–2016 GSL Brine Database (Rupke and Mcdonald, 2012). In **A**, note that aragonite is undersaturated (i.e., aragonite dissolution is favored) with respect to aqueous solute composition in solutions with pH < 7.0 in both the NA and SA, while dolomite remains saturated (i.e., dolomite precipitation is favored) in solutions with pH > 5.5 in the NA and pH > 6.0 in the SA. In **B**, note that aragonite only becomes undersaturated under extreme conditions (minimum alkalinity and low temperatures), while dolomite remains saturated under all observed conditions. Values plotted in **A** are presented in **Supplementary Table S5** and values plotted in **B** are presented in **Supplementary Table S3**.

FIGURE 7 | Proposed model for the formation of aragonite and dolomite in mats and sediments in Great Salt Lake (GSL). Photosynthesis in benthic cyanobacterial mats generates a local increase in alkalinity, promoting the precipitation of aragonite on extracellular polymeric substances, as well as generating large quantities of biomass and O_2. Aerobic heterotrophs oxidize sufficient biomass and photosynthate to deplete local O_2, generating a niche for anaerobic fermentative bacteria and sulfate-reducing bacteria (SRB). Organic acids produced by fermenters both lower porewater pH, promoting aragonite dissolution, and provide substrates supporting heterotrophic SRB in underlying sediments. SRB activity promotes dolomite precipitation in mildly acidic microenvironments where aragonite precipitation is thermodynamically disfavored. Abbreviations: Ar, aragonite; Do, dolomite; Cyano, cyanobacteria; Het, aerobic heterotrophic bacteria; Ferm, fermentative bacteria; SRB, sulfate-reducing bacteria.

processes. However, 16S rRNA gene (Lindsay et al., 2017, 2019) and metagenomic sequence (E.S. Boyd, *unpublished data*) do not reveal abundant populations inferred to be SRBs (< 2% of total community) in benthic phototrophic microbial mats associated with microbialites from Bridger Bay. We therefore propose a modification to the model put forth by Pace et al. (2016) which may also help to explain the distribution of aragonite and protodolomite in GSL (*see* **Figure 7**). Like the previous model, we suggest aragonite precipitation takes place in photosynthetic microbial mats due to a localized increase in alkalinity and this aragonite is then deposited into benthic sediments. However, the increase in alkalinity is proposed to be induced by photosynthetic CO_2 consumption rather than the activity of low abundance SRBs. This interpretation is consistent with previous studies showing that oxygenic photosynthetic organisms can precipitate
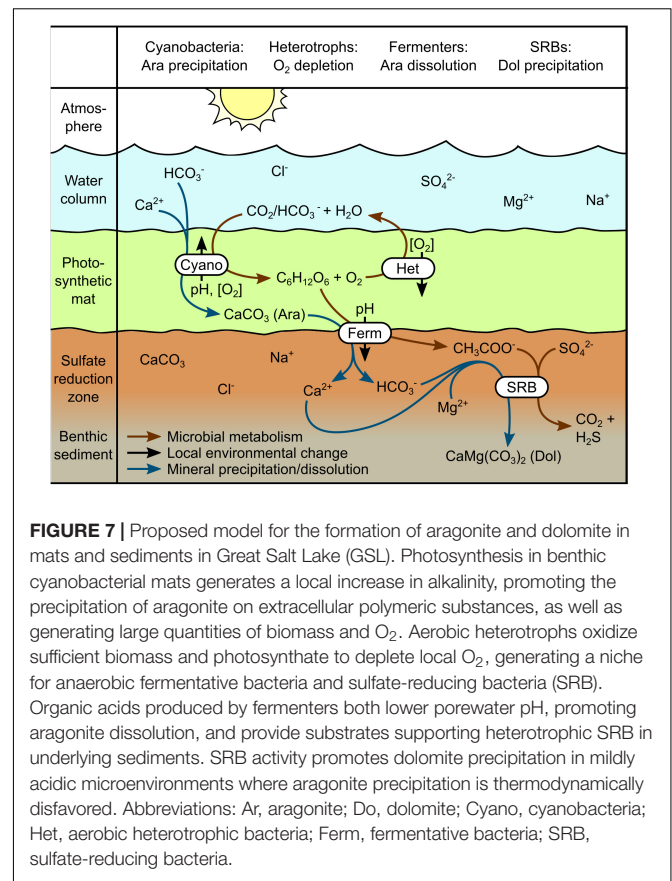
aragonite through localized increases in alkalinity (Merz, 1992; Al-Horani et al., 2003; Kranz et al., 2010).

Also like the previous model, we suggest that partial dissolution of aragonite occurs as a result of the activities of fermentative organisms inhabiting benthic mats and sediments. These organisms produce organic acids as waste, lowering local pH to a level that favors dissolution of aragonite, but not dolomite (**Figures 6A**, **7**). Based on available data, it is unclear whether fermentation takes place in the mats or the sediment column. However, numerous species of *Clostridia*, a genus commonly known for fermentation (Rainey et al., 2015), have been detected in previous molecular characterizations of benthic cyanobacterial mats from the SA of GSL (Lindsay et al., 2017, 2019). It has been suggested that Mg^{2+} ions also need to be released to allow for dolomite to form (Pace et al., 2016). However, the Mg^{2+}:Ca^{2+} ratios of waters in both the SA and NA do vary seasonally and have been > 20 since 1966 (Rupke and Mcdonald, 2012), which should be favorable for (proto)dolomite formation (Folk and Land, 1975).

Finally, in the slightly acidic microenvironments created by the activities of fermentative bacteria, where aragonite precipitation is thermodynamically unfavorable, the activities of SRBs promote the formation of VHMC and protodolomite (Pace et al., 2016). We suggest that the dolomite in the SA core is likely authigenic and primary, since it has never experienced deep burial and the transformation of aragonite to dolomite is

sluggish at temperatures common to GSL (0–32°C; **Figure 6B**) due to kinetic constraints (Machel and Mountjoy, 1986). This is supported by SEM images from the SA sediment core (**Figure 4**) that show that the protodolomite is euhedral and displays no aragonite pseudomorph, features that suggest it is not a dolomitization product of aragonite.

Potential Controls on the Formation of Protodolomite in GSL

While elucidating the precise mechanisms of protodolomite precipitation is beyond the scope of this study, some inferences can be made from the data presented. A commonly proposed model for dolomite formation in brines rich in $MgSO_4$ involves depletion of SO_4^{2-} by SRB, which is thought to reduce ion pairing with Mg^{2+} and make the latter more readily available for incorporation into carbonate lattices (Baker and Kastner, 1981; Vasconcelos and Mckenzie, 1997; Warthmann et al., 2000; Bontognali et al., 2010). However, our SA sediment core, which is rich in protodolomite, exhibits SO_4^{2-} concentrations exceeding 40 mM throughout (**Supplementary Table S7** and **Figure 5**), indicating that substantial depletion of SO_4^{2-} via SR activity is unlikely to be responsible for protodolomite formation in this system.

Alternatively, most current hypotheses for sedimentary dolomite formation require the presence of a catalyst such as dioxane (Oomori and Kitano, 1987), methane (Xu, 2010; Zhang et al., 2010), polysaccharides (Zhang et al., 2012b; Shen et al., 2015), EPS (Shen et al., 2015; Huang et al., 2019), dissolved sulfide (Zhang et al., 2012a, 2013; Shen et al., 2014; Lu et al., 2018), or clays (Liu et al., 2019). The presence of a catalyst may help lower the dehydration energy of Mg^{2+}-water complexes and allow crystal nucleation and growth (Lippmann, 1973; De Leeuw and Parker, 2001; Gregg et al., 2015). Importantly, the lack of (proto)dolomite in all of our microbial mat samples suggests polysaccharides and EPS are unlikely to control micritic dolomite precipitation in GSL, as these molecules are abundant in such mats (Bolhuis et al., 2014). The clay smectite was detected in both the NA and SA sediment column while protodolomite was largely restricted to the SA core. This set of observations discounts the probability of clays as a potential catalyst. Another potential catalyst is dissolved sulfide, present in high concentrations (∼500 µM) in the top most sections of the SA core. Previous studies demonstrate that dissolved sulfide can promote Mg^{2+} incorporation and dolomite nucleation (Zhang et al., 2012a, 2013; Shen et al., 2014).

Sulfide concentrations of 500 µM, as found in the top section of the SA sediment core (**Figure 5**), are sufficient to lower the dehydration energy of Mg^{2+}-water complexes and promote fast nucleation of HMC in Mg-rich solutions (Zhang et al., 2013). The zone of elevated sulfide in the SA core corresponds with a high abundance of 16S rRNA gene transcripts affiliated with the SRB *D. utahense* (98% nucleotide identity), previously isolated from the NA of GSL (Jakobsen et al., 2006) (**Figure 5**). *D. utahense* is a heterotroph that can

use a variety of organic substrates to support SR, including the fermentation product acetate when H_2 is also provided (Jakobsen et al., 2006). Consistent with an abundance of *D. utahense* transcripts in the top section of the SA core, rates of acetate assimilation/mineralization were highest in the top section of the SA core and dissolved H_2 concentrations increased with depth in the SA core, suggesting a net sink for H_2 in the near surface sediments (**Figure 5**). Finally, the concentration of sulfide in the SA core was positively correlated with the abundance of transcripts attributable to *D. utahense* (Pearson $R = 0.99$, $p < 0.01$). This is consistent with other hypersaline intertidal areas, where active zones of SR are localized near the sediment–water interface (Van Lith et al., 2002). Together, these observations strongly suggest the presence of an active SR zone near the SA sediment–water interface, where protodolomite was detected in appreciable quantities (≥20% of sediment) despite being absent from overlying mats (**Figure 2**).

In contrast to the SA, evidence for an active SR zone in the NA core is lacking and protodolomite is scarce (**Figure 2B** and **Supplementary Table S6**). The primary SRB in the NA was related to *D. autotrophicus*, which requires H_2 or formate as an electron donor, but can grow either heterotrophically or autotrophically (Mayilraj et al., 2009). Despite the presence of this putatively autotrophic and hydrogenotrophic SRB, variance in sulfide concentration and CO_2 assimilation activity with depth was not observed in NA sediment porewaters (**Figure 5**). Moreover, the abundance of transcripts attributable to *D. autotrophicus* was not correlated with the concentration of sulfide and these sediments did not appear to be a sink for H_2 (**Figure 5**). It is possible that these cells are minimally active and are in a maintenance mode of metabolism due to salinity stress, a conclusion that would be consistent with previously compiled data on the activity and abundance of SRB in the NA versus the SA (Brandt et al., 2001; Boyd et al., 2017). In any case, the lack of an active SR zone in the NA corresponds with the relative scarcity of protodolomite in the NA sediment core.

Thus, even though the mechanisms of protodolomite precipitation remain unclear, we infer that the activity of SRB is at least one important control on this process in GSL sediments. The biotic and abiotic controls on the activities of SRB may then be expected to affect the formation of protodolomite as well. One such control that may be important is the abundance of nutrient-rich organic carbon, and by extension the activity of benthic photosynthetic communities. Benthic phototrophic microbial mats are ubiquitous in the SA of GSL, either associated with microbialites or in shallow marginal areas of the lake without microbialites. Overall, these mats contribute up to 30% of the total productivity in the SA (Wurtsbaugh et al., 2011). In contrast to the SA, phototrophic mats are conspicuously absent in the NA of GSL (Lindsay et al., 2017). Moreover, the total biomass associated with microbialites sampled from the SA (as estimated by ribosomal RNA gene abundances) was three orders of magnitude greater than in the NA. These observations were attributed to constraints imposed by high salinity on the primary architect and the primary producer of these mats, Cyanobacteria (Wurtsbaugh et al., 2011) within

the genus *Euhalothece* (Lindsay et al., 2017, 2019) which grow sub-optimally or not at all at salinities that exceed ~20% (Garcia-Pichel et al., 1998).

Not only the abundance of organic matter but also its quality may be important in promoting or constraining the growth of SRB. Organic matter in the top-most sediments in the SA sediment core had a C:N ratio of ~4 (**Figure 5**), which is consistent with fresh photosynthetic biomass. In contrast, the C:N ratio of organic matter in the NA core was ~25 throughout. High C:N ratios have been suggested to indicate input of terrestrial soil or vascular plant material (Prahl et al., 1994). However, since these ratios were not observed in the SA sediment core, where most riverine sediment input takes place, we suggest that in the NA they more likely reflect substantial processing by microorganisms and slow-to-negligible fresh biomass deposition. Thus, salinity may place constraints on the abundance of primary producers and their activity, which in turn influences production of biomass that can support heterotrophic activity, such as fermentation and SR. High salinities also inhibit the growth of *D. utahense*, which grows optimally at a salinity of 8-10% NaCl, near to that of SA sediment porewaters (13.1–16.5%). Differences in salinity between the NA and SA of GSL may thus contribute to differential growth of both SRB and the Cyanobacteria on which they depend for organic carbon.

Unlike the NA sediment core, both the NAN-1 and NAN-2 hand samples were high in nitrogen-rich organic matter (C:N ratios of 7 and 11). Given the absence of benthic phototrophic mats at this sampling location and in the NA in general, this organic matter is interpreted to represent allochthonous input from down slope surface runoff to this playa location. This suggests that sediment characteristics imposed by depositional environment may represent an additional control on the formation of protodolomite. One such characteristic of both the NA core and NAN-1 sediments that provides information about their depositional environment is the abundance of oolitic sand. Oolitic sands tend to accumulate in wave agitated waters (Pedone and Norgauer, 2002). Together with hypersalinity, high-energy (e.g., wave agitated) depositional environments may physically constrain the development of robust phototrophic mats and SR zones capable of promoting protodolomite formation. Moreover, oolitic sediments such as those identified in NAN-1 and the NA sediment core also tend to have high porosity (Choquette and Pray, 1970). This could more easily allow infusion of oxic waters to greater sediment column depths, which would inhibit the development of an SR zone due to the O_2 sensitivity of SRB (Postgate, 1979). The contrasting sediment compositions of NAN-1 and NAN-2 indicate that slight differences in location can lead to substantial differences in wave energy and sediment characteristics. Moreover, the presence of protodolomite in the NAN-2 sample suggests these differences may be as important as salinity in constraining the formation of protodolomite, given that salinity is expected to be relatively uniform on the scale (meters) that separated the NAN-1 and NAN-2 samples. Further investigation of the distribution of protodolomite and the microbiology and porewater geochemistry of sediments from a range of depositional settings in GSL may help in further evaluating this hypothesis.

CONCLUSION

The detection of aragonite as the primary carbonate mineral in photosynthetic mats from the SA of GSL, without the presence of abundant SRB, suggests that oxygenic photosynthesis and corresponding alkalinity increases are responsible for aragonite formation. The detection of protodolomite rather than aragonite as the primary carbonate mineral in sediment cores from the SA suggests primary protodolomite precipitation in benthic sediments, where the lowest organic C:N ratios (indicative of deposition of fresh photosynthetic biomass), the highest rates of acetate transformation, the highest abundance of SRB-associated gene transcripts, and the highest concentrations of sulfide occur. This suggests that deposition of photosynthetic biomass through a zone of active heterotrophic SR in underlying sediments is likely to be a primary variable favoring the formation of protodolomite. Following the model of Pace et al. (2016) and consistent with the general function of microbial mat ecosystems, the deposited organic matter is first oxidized and/or fermented, generating anoxia, organic acids, and localized zones of acidity. This leads to two outcomes, partial dissolution of detrital aragonite and stimulation of SRBs, that together promote protodolomite formation. The comparative lack of protodolomite in the NA sediment core is suggested to result from constraints imposed by extreme hypersalinity and depositional environment that together limit the development of productive phototrophic mats and, in turn, suppress the activities of fermenters and SRBs. Importantly, the detection of protodolomite in the NAN-2 hand sample, which had a high abundance of fresh organic carbon, suggests that the photosynthate that drives the development of an SR zone and that is putatively responsible for the formation of this mineral may not need to be autochthonous.

The protodolomite identified in the SA sediment core exhibits euhedral microtextures nucleating on aragonite surfaces. While SRB were present in the uppermost segments of the NA core, high sulfide concentrations and similar euhedral dolomite microtextures were not observed, suggesting that the presence of SRB alone is insufficient to promote formation of these mineral structures, at least at low abundances such as those observed in the NA core. We suggest that additional key factors promoting protodolomite formation arise due to the productivity of photosynthetic benthic mats, including heterotrophy-driven anoxia, fermentation-derived acidity decreasing the saturation index of aragonite, and heterotrophic SR with accompanying high concentrations of dissolved sulfide. Importantly, such conditions favorable for protodolomite formation may not develop in high energy environments due to the potential to physically remove photosynthetic mats or to create conditions (e.g., high porosity oolitic sands) that otherwise do not favor the development of an SR zone.

DATA AVAILABILITY STATEMENT

Raw reads, quality scores, and mapping files for the archaeal and bacterial 16S rRNA gene transcript libraries have been deposited

in the NCBI Short Reads Archive under BioProject accession number PRJNA481529.

AUTHOR CONTRIBUTIONS

ED, EF, YF, ML, CS, NF, MW, AW, and DC collected data. DM and HX oversaw XRD analyses. BB and AR assisted with sample collection. DL and EB oversaw the project. All authors contributed to data analysis and interpretation. ED, EF, and EB wrote the manuscript.

FUNDING

SUPPLEMENTARY MATERIAL

The Supplementary Material for this article can be found online at: https://www.frontiersin.org/articles/10.3389/feart.2020.00024/full#supplementary-material

REFERENCES

Alderman, A. R. (1958). Aspects of carbonate sedimentation. *J. Geol. Soc. Aust.* 6, 1–10. doi: 10.1080/00167615808728491

Al-Horani, F. A., Al-Moghrabi, S. M., and De Beer, D. (2003). The mechanism of calcification and its relation to photosynthesis and respiration in the scleractinian coral *Galaxea fascicularis*. *Mar. Biol.* 142, 419–426. doi: 10.1007/s00227-002-0981-8

Baker, P. A., and Kastner, M. (1981). Constraints on the formation of sedimentary dolomite. *Science* 213, 214–216. doi: 10.1126/science.213.4504.214

Baskin, R. L. (2014). *Occurrence and Spatial Distribution of Microbial Bioherms in Great Salt Lake, Utah*. Salt Lake City, UT: University of Utah.

Baxter, B. K., Litchfield, C. D., Sowers, K., Griffith, J. D., Dassarma, P. A., and Dassarma, S. (eds) (2005). *Microbial diversity of Great Salt Lake*. Dordrecht: Springer.

Belovsky, G. E., Stephens, D., Perschon, C., Birdsey, P., Paul, D., Naftz, D., et al. (2011). The great salt lake ecosystem (Utah, USA): long term data and a structural equation approach. *Ecosphere* 2, 1–40. doi: 10.1890/ES10-00091.1

Bolhuis, H., Cretoiu, M. S., and Stal, L. J. (2014). Molecular ecology of microbial mats. *FEMS Microbiol. Ecol.* 90, 335–350. doi: 10.1111/1574-6941.12408

Bontognali, T. R. R., Vasconcelos, C., Warthmann, R. J., Bernasconi, S. M., Dupraz, C., Strohmenger, C. J., et al. (2010). Dolomite formation within microbial mats in the coastal sabkha of Abu Dhabi (United Arab Emirates). *Sedimentology* 57, 824–844. doi: 10.1111/j.1365-3091.2009.01121.x

Bouton, A., Vennin, E., Boulle, J., Pace, A., Bourillot, R., Thomazo, C., et al. (2016). Linking the distribution of microbial deposits from the Great Salt Lake (Utah, USA) to tectonic and climatic processes. *Biogeosciences* 13, 5511–5526. doi: 10.5194/bg-13-5511-2016

Boyd, E. S., Yu, R.-Q., Barkay, T., Hamilton, T. L., Baxter, B. K., Naftz, D. L., et al. (2017). Effect of salinity on mercury methylating benthic microbes and their activities in Great Salt Lake. *Utah. Sci. Total Environ.* 58, 495–506. doi: 10.1016/j.scitotenv.2016.12.157

Brandt, K. K., Vester, F., Jensen, A. N., and Ingvorsen, K. (2001). Sulfate reduction dynamics and enumeration of sulfate-reducing bacteria in hypersaline sediments of the Great Salt Lake (Utah, USA). *Microb. Ecol.* 41, 1–11. doi: 10.1007/s002480000059

Burlage, R. S., Atlas, R., Stahl, D., Geesey, G., and Sayler, G. (eds) (1998). *Microbes of the SuIfur CycIe*. New York, NY: Oxford.

Cannon, J. S., and Cannon, M. A. (eds) (2002). *The Southern Pacific Railroad Trestle – Past and Present*. . Salt Lake City, UT: Utah Department of Natural Resources.

Choquette, P. W., and Pray, L. C. (1970). Geologic nomenclature and classification of porosity in sedimentary carbonates. *AAPG Bull.* 54, 207–250. doi: 10.1306/5d25c98b-16c1-11d7-8645000102c1865d

Colman, S. M., Kelts, K. R., and Dinter, D. A. (2002). Depositional history and neotectonics in Great Salt Lake, Utah, from high-resolution seismic stratigraphy. *Sediment. Geol.* 148, 61–78. doi: 10.1016/S0037-0738(01)00210-X

De Leeuw, N. H., and Parker, S. C. (2001). Surface–water interactions in the dolomite problem. *Physi. Chem. Chem. Phys.* 3, 3217–3221. doi: 10.1039/B102928M

Eardley, A. J. (1938). Sediments of Great Salt Lake, Utah. *AAPG Bull.* 22, 105–120. doi: 10.1306/3D9330DE-16B1-11D7-8645000102C1865D

Fairbridge, R. W. (1957). "The Dolomite Question," in *Regional Aspects of Carbonate Deposition*, eds R. J. L. Blanc, and J. G. Breeding, (Tulsa, PA: SEPM Society for Sedimentary Geology).

Fang, Y., and Xu, H. (2019). A new approach to quantify the ordering state of protodolomite using XRD, TEM, and Z-contrast imaging. *J. Sediment. Res.* 89, 537–551. doi: 10.2110/jsr.2019.29

Fendinger, N. J., and Adams, D. D. (1986). A headspace equilibration technique for measurement of dissolved gases in sediment pore water. *Int. J. Environ. Anal. Chem.* 23, 253–265. doi: 10.1080/03067318608076449

Fogo, J. K., and Popowsky, M. (1949). Spectrophotometric eetermination of hydrogen sulfide - Methylene blue method. *Anal. Chem.* 21, 732–734. doi: 10.1021/ac60030a028

Folk, R. L., and Land, L. S. (1975). Mg/Ca ratio and salinity; two controls over crystallization of dolomite. *AAPG Bull.* 59, 60–68. doi: 10.1306/83d91c0e-16c7-11d7-8645000102c1865d

Garcia-Pichel, F., Nubel, U., and Muyzer, G. (1998). The phylogeny of unicellular, extremely halotolerant cyanobacteria. *Arch. Microbiol.* 169, 469–482. doi: 10.1007/s002030050599

Graf, D. L., and Goldsmith, J. R. (1956). Some hydrothermal syntheses of dolomite and protodolomite. *J. Geol.* 64, 173–186. doi: 10.1086/626332

Gregg, J. M., Bish, D. L., Kaczmarek, S. E., and Machel, H. G. (2015). Mineralogy, nucleation and growth of dolomite in the laboratory and sedimentary environment: a review. *Sedimentology* 62, 1749–1769. doi: 10.1111/sed.12202

Gwynn, J. W. (1980). *Great salt lake: A Scientific, Historical, and Economic Overview*. Salt Lake City, UT: Utah Geological and Mineral Survey.

Gwynn, J. W. (1996). *Commonly Asked Questions About Utah's Great Salt Lake and Ancient Lake Bonneville*. Salt Lake City, UT: Utah Geological Survey.

Gwynn, J. W. (2007). *Great Salt Lake Brine Chemistry Databases & Reports 1966-2006*. Salt Lake City, UT: Utah Geological Survey.

Hamilton, T. L., Peters, J. W., Skidmore, M. L., and Boyd, E. S. (2013). Molecular evidence for an active endogenous microbiome beneath glacial ice. *ISME J.* 7, 1402–1412. doi: 10.1038/ismej.2013.31

Hardie, L. A. (1987). Dolomitization; a critical view of some current views. *J. Sediment,. Res.* 57, 166–183. doi: 10.1306/212F8AD5-2B24-11D7-8648000102C1865D

Hassibe, W. R., and Keck, W. G. (1991). "The Great Salt Lake," in *General Information Product*, (Washington, D.C: Geological Survey).

Huang, Y.-R., Yao, Q.-Z., Li, H., Wang, F.-P., Zhou, G.-T., and Fu, S.-Q. (2019). Aerobically incubated bacterial biomass-promoted formation of disordered dolomite and implication for dolomite formation. *Chem. Geol.* 523, 19–30. doi: 10.1016/j.chemgeo.2019.06.006

Jakobsen, T. F., Kjeldsen, K. U., and Ingvorsen, K. (2006). *Desulfohalobium utahense* sp. nov., a moderately halophilic, sulfate-reducing bacterium isolated from Great Salt Lake. *Int.; J. Syst. Evol. Microbiol.* 56, 2063–2069. doi: 10.1099/ijs.0.64323-0

Jones, B. F., Naftz, D. L., Spencer, R. J., and Oviatt, C. G. (2009). Geochemical evolution of great salt lake. Utah, USA. *Aquat. Geochem.* 15, 95–121. doi: 10.1007/s10498-008-9047-y

Kenward, P. A., Goldstein, R. H., González, L. A., and Roberts, J. A. (2009). Precipitation of low-temperature dolomite from an anaerobic microbial consortium: the role of methanogenic Archaea. *Geobiology* 7, 556–565. doi: 10.1111/j.1472-4669.2009.00210.x

Kranz, S. A., Gladrow, D. W., Nehrke, G., Langer, G., and Rosta, B. (2010). Calcium carbonate precipitation induced by the growth of the marine cyanobacteria *Trichodesmium*. *Limnol. Oceanogr.* 55, 2563–2569. doi: 10.4319/lo.2010.55.6.2563

Lindsay, M. R., Amenabar, M. J., Fecteau, K. M., Debes, R. V., Fernandes Martins, M. C., Fristad, K. E., et al. (2018). Subsurface processes influence oxidant availability and chemoautotrophic hydrogen metabolism in Yellowstone hot springs. *Geobiology* 16, 674–692. doi: 10.1111/gbi.12308

Lindsay, M. R., Anderson, C., Fox, N., Scofield, G., Allen, J., Anderson, E., et al. (2017). Microbialite response to an anthropogenic salinity gradient in Great Salt Lake. *Utah. Geobiol.* 15, 131–145. doi: 10.1111/gbi.12201

Lindsay, M. R., Johnston, R. E., Baxter, B. K., and Boyd, E. S. (2019). Effects of salinity on microbialite-associated production in Great Salt Lake. *Utah. Ecol.* 100:e02611. doi: 10.1002/ecy.2611

Lippmann, F. (1973). *Sedimentary Carbonate Minerals*. New York: Springer Verlag.

Liu, D., Xu, Y., Papineau, D., Yu, N., Fan, Q., Qiu, X., et al. (2019). Experimental evidence for abiotic formation of low-temperature proto-dolomite facilitated by clay minerals. *Geochim. Cosmochim. Acta* 247, 83–95. doi: 10.1016/j.gca.2018.12.036

Lu, Y., Sun, X., Xu, H., Konishi, H., Lin, Z., Xu, L., et al. (2018). Formation of dolomite catalyzed by sulfate-driven anaerobic oxidation of methane: mineralogical and geochemical evidence from the northern South China Sea. *Am. Mineral.* 103, 720–734. doi: 10.2138/am-2018-6226

Macdonald, M. L., Wadham, J. L., Telling, J., and Skidmore, M. L. (2018). Glacial erosion liberates lithologic energy sources for microbes and acidity for chemical weathering beneath glaciers and ice sheets. *Front. Earth Sci.* 6:212. doi: 10.3389/feart.2018.00212

Machel, H.-G., and Mountjoy, E. W. (1986). Chemistry and environments of dolomitization — A reappraisal. *EarthSci. Rev.* 23, 175–222. doi: 10.1016/0012-8252(86)90017-6

Mayilraj, S., Kaksonen, A. H., Cord-Ruwisch, R., Schumann, P., Sproer, C., Tindall, B. J., et al. (2009). *Desulfonauticus autotrophicus* sp. nov., a novel thermophilic sulfate-reducing bacterium isolated from oil-production water and emended description of the genus Desulfonauticus. *Extremophiles* 13, 247–255. doi: 10.1007/s00792-008-0212-4

Merz, M. U. E. (1992). The biology of carbonate precipitation by cyanobacteria. *Facies* 26, 81–101. doi: 10.1007/bf02539795

Moore, T. S., Murray, R. W., Kurtz, A. C., and Schrag, D. P. (2004). Anaerobic methane oxidation and the formation of dolomite. *Earth Planet. Sci. Lett.* 229, 141–154. doi: 10.1016/j.epsl.2004.10.015

Oomori, T., and Kitano, Y. (1987). Synthesis of protodolomite from sea water containing dioxane. *Geochem. J.* 21, 59–65. doi: 10.2343/geochemj.21.59

Oren, A. (2013). "Life at High Salt Concentrations," in *The Prokaryotes*, eds M. Falkow, S. Rosenberg, E. Schleifer, and K.-H. Stackebrandt, (Berlin: Springer), 421–440. doi: 10.1007/978-3-642-30123-0_57

Pace, A., Bourillot, R., Bouton, A., Vennin, E., Galaup, S., Bundeleva, I., et al. (2016). Microbial and diagenetic steps leading to the mineralisation of Great Salt Lake microbialites. *Sci. Rep.* 6:31495. doi: 10.1038/srep31495

Parkhurst, D., and Appelo, T. (2013). *Description of Input and Examples for PHREEQC Version 3—a Computer Program for Speciation, Batch-Reaction, One-Dimensional Transport, and Inverse Geochemical Calculations*. Scotts Valley, CA: Createspace Independent Publication.

Pedone, V. A., and Norgauer, C. H. (2002). *Petrology and Geochemistry of Recent Ooids From the Great Salt Lake, Utah. Salt*. Lake City, UT: Utah Department of Natural Resources.

Post, F. J. (1977). The microbial ecology of the Great Salt Lake. *Microb. Ecol.* 3, 143–165. doi: 10.1007/BF02010403

Post, F. J. (1981). "Microbiology of the Great Salt Lake north arm," in *Salt Lakes*, ed. J. Wallace Gwynn, (Dordrecht: Springer), 59–69. doi: 10.1007/978-94-009-8665-7_6

Postgate, J. R. (1979). *The Sulphate-Reducing Bacteria*. Cambridge: Cambridge University Press.

Prahl, F. G., Ertel, J. R., Goni, M. A., Sparrow, M. A., and Eversmeyer, B. (1994). Terrestrial organic carbon contributions to sediments on the Washington margin. *Geochim. Cosmochim. Acta* 58, 3035–3048. doi: 10.1016/0016-7037(94)90177-5

Rainey, F. A., Hollen, B. J., and Small, A. M. (2015). "Clostridium," in *Bergey's Manual of Systematics of Archaea and Bacteria*, eds W. B. Whitman, F. Rainey, P. Kämpfer, M. Trujillo, J. Chun, P. Devos, et al. (Hoboken, NJ: Wiley), 1–122.

Reeder, R. J., and Sheppard, C. E. (1984). Variation of lattice parameters in some sedimentary dolomites. *Am. Mineral.* 69, 520–527.

Reid, R. P., Visscher, P. T., Decho, A. W., Stolz, J. F., Bebout, B. M., Dupraz, C., et al. (2000). The role of microbes in accretion, lamination and early lithification of modern marine stromatolites. *Nature* 406:989. doi: 10.1038/35023158

Rosenberg, P. E., Burt, D. M., and Holland, H. D. (1967). Calcite-dolomite-magnesite stability relations in solutions: The effect of ionic strength. *Geochim. Cosmochim. Acta* 31, 391–396. doi: 10.1016/0016-7037(67)90049-X

Rosenberg, P. E., and Holland, H. D. (1964). Calcite-dolomite-magnesite stability relations in solutions at elevated temperatures. *Science* 145, 700–701. doi: 10.1126/science.145.3633.700

Rupke, A., and Mcdonald, A. (2012). *Great Salt Lake Brine Chemistry Database, 1966–2011*. Open File Report 596. Salt Lake City, UT: Utah Geological Survey.

Saini-Eidukat, B., and Yahin, A. (1999). Web-phreeq: a WWW instructional tool for modeling the distribution of chemical species in water[2]. *Comput. Geosci.* 25, 347–353. doi: 10.1016/S0098-3004(98)00138-1

Schloss, P. D., Westcott, S. L., Ryabin, T., Hall, J. R., Hartmann, M., Hollister, E. B., et al. (2009). Introducing mothur: Open-source, platform-independent, community-supported software for describing and comparing microbial communities. *Appl. Environ. Microbiol.* 75, 7537–7541. doi: 10.1128/AEM.01541-09

Schneider, D., Arp, G., Reimer, A., Reitner, J., and Daniel, R. (2013). Phylogenetic analysis of a microbialite-forming microbial mat from a hypersaline lake of the Kiritimati Atoll. Central Pacific. *PLoS One* 8:e66662. doi: 10.1371/journal.pone.0066662

Shen, Z., Liu, Y., Brown, P. E., Szlufarska, I., and Xu, H. (2014). Modeling the effect of dissolved hydrogen sulfide on Mg2+–water complex on dolomite {104} surfaces. *J. Phys. Chem. C* 118, 15716–15722. doi: 10.1021/jp5028417

Shen, Z., Szlufarska, I., Brown, P. E., and Xu, H. (2015). Investigation of the role of polysaccharide in the dolomite growth at low temperature by using atomistic simulations. *Langmuir* 31, 10435–10442. doi: 10.1021/acs.langmuir.5b02025

Spear, J. R., Walker, J. J., Mccollom, T. M., and Pace, N. R. (2005). Hydrogen and bioenergetics in the Yellowstone geothermal ecosystem. *Proc. NatL. Acad. Sci. U. S. A.* 102, 2555–2560. doi: 10.1073/pnas.0409574102

Stephens, D. W. (1990). Changes in lake levels, salinity and the biological community of Great-Salt-Lake (Utah. USA), 1847–1987. *Hydrobiologia* 197, 139–146. doi: 10.1007/978-94-009-0603-7_13

Stephens, D. W., and Gillespie, D. M. (1976). Phytoplankton production in the Great Salt Lake, Utah, and a laboratory study of algal response to enrichment1. *Limnol. Oceanogr.* 21, 74–87. doi: 10.4319/lo.1976.21.1.0074

Survey, U. G. (2013). *Quaternary Fault and Fold Database and Map of Utah*. Montevideo: UAGR Center.

Urschel, M. R., Kubo, M. D., Hoehler, T. M., Peters, J. W., and Boyd, E. S. (2015). Carbon source preference in chemosynthetic hot spring communities. *Appl. Environ. Microbiol.* 81, 3834–3847. doi: 10.1128/AEM.00511-15

Van Lith, Y., Vasconcelos, C., Warthmann, R., Martins, J. C. F., and Mckenzie, J. A. (2002). Bacterial sulfate reduction and salinity: two controls on dolomite precipitation in Lagoa Vermelha and Brejo do Espinho (Brazil). *Hydrobiologia* 485, 35–49. doi: 10.1023/A:1021323425591

Vasconcelos, C., and Mckenzie, J. A. (1997). Microbial mediation of modern dolomite precipitation and diagenesis under anoxic conditions (Lagoa Vermelha, Rio de Janeiro, Brazil). *J. Sedimen. Res.* 67, 378–390. doi: 10.1306/D4268577-2B26-11D7-8648000102C1865D

Vasconcelos, C., Mckenzie, J. A., Bernasconi, S., Grujic, D., and Tiens, A. J. (1995). Microbial mediation as a possible mechanism for natural dolomite formation at low temperatures. *Nature* 377:220. doi: 10.1038/377220a0

Wang, Q., Garrity, G. M., Tiedje, J. M., and Cole, J. R. (2007). Naive Bayesian classifier for rapid assignment of rRNA sequences into the new bacterial taxonomy. *Appl. Environ. Microbiol.* 73, 5261–5267. doi: 10.1128/AEM. 00062-07

Warthmann, R., Van Lith, Y., Vasconcelos, C., Mckenzie, J. A., and Karpoff, A. M. (2000). Bacterially induced dolomite precipitation in anoxic culture experiments. *Geology* 28, 1091–1094. doi: 10.1130/0091-7613(2000)028<1091: bidpia>2.3.co;2

Wells, A. J. (1962). Recent dolomite in the Persian Gulf. *Nature* 194:274. doi: 10.1038/194274a0

Wurtsbaugh, W. A., Gardberg, J., and Izdepski, C. (2011). Biostrome communities and mercury and selenium bioaccumulation in the Great Salt Lake (Utah. USA). *Sci. Total Environ.* 409, 4425–4434. doi: 10.1016/j.scitotenv.2011. 07.027

Xu, H. (2010). "Synergistic roles of microorganisms in mineral precipitates associated with deep sea methane seeps," in *Geomicrobiology: Molecular and Environmental Perspective*, eds L. L. Barton, M. Mandl, and A. Loy, (Dordrecht: Springer), 325–346. doi: 10.1007/978-90-481-9204-5_15

Zhang, F., Xu, H., Konishi, H., Kemp, J. M., Roden, E. E., and Shen, Z. (2012a). Dissolved sulfide-catalyzed precipitation of disordered dolomite: Implications for the formation mechanism of sedimentary dolomite. *Geochim. Cosmochim. Acta* 97, 148–165. doi: 10.1016/j.gca.2012. 09.008

Zhang, F., Xu, H., Konishi, H., and Roden, E. E. (2010). A relationship between d104 value and composition in the calcite-disordered dolomite solid-solution series. *Am. Mineral.* 95, 1650–1656. doi: 10.2138/am.2010.3414

Zhang, F., Xu, H., Konishi, H., Shelobolina, E. S., and Roden, E. E. (2012b). Polysaccharide-catalyzed nucleation and growth of disordered dolomite: a potential precursor of sedimentary dolomite. *Am. Mineral.* 97, 556–567. doi: 10.2138/am.2012.3979

Zhang, F., Yan, C., Teng, H. H., Roden, E. E., and Xu, H. (2013). In situ AFM observations of Ca–Mg carbonate crystallization catalyzed by dissolved sulfide: implications for sedimentary dolomite formation. *Geochim. Cosmochim. Acta* 105, 44–55. doi: 10.1016/j.gca.2012.11.010